

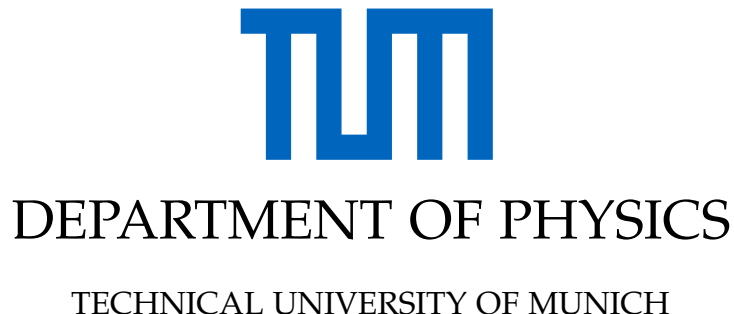


Bachelor's Thesis in Physics

Determination of the Spectrum of Remoderated Positrons

Julius Hussl





Bachelor's Thesis in Physics

Determination of the Spectrum of Remoderated Positrons

Bestimmung des Spektrums remoderierter Positronen

Author: Julius Hussl
Supervisor: Prof. Dr. Christoph Hugenschmidt
Advisor: Dr. Francesco Guatieri
Submission Date: 29/08/2025



I hereby confirm that this bachelor's thesis in physics is my own work and I have documented all sources and material used.

Garching, 29/08/2025

Julius Hussl

Abstract

The quality of monoenergetic positron beams, essential for surface science and depth-resolved defect studies, is fundamentally determined by the energy spectrum of the positrons reemitted from a moderator. This thesis details the development and implementation of a new experimental apparatus designed to precisely determine this spectrum. A Retarding Field Analyzer (RFA) was designed and integrated into the Setup for Low-Energy Positron Experiments (SLOPE) at TUM. A central component of this work was the construction of a galvanically isolated active sampleholder, which utilizes a custom, on-board DC-DC charge pump regulated by a PID control loop to provide a stable and precise bias voltage to the retarding grid. Functionality of the new system was demonstrated through a series of measurements on single-crystal tungsten, nickel, and platinum samples. A clear reemission signal was observed from W(111), yielding a maximum kinetic energy of $1.87(10)$ eV. This value being lower than the accepted literature value, along with the broad shape of the energy spectrum, suggests the influence of surface contaminants and contact potentials within the apparatus. Measurements of energy-dependent reemission yields follow the expected trend of higher yields at lower implantation energies; a particularly steep increase at the lowest energies suggests a significant contribution from epithermal positrons, while artifacts related to beam transport optics were also identified. This work successfully establishes a functional setup for retarding field analysis of remoderated positrons at SLOPE. The initial results highlight the capabilities of the system while also identifying key areas for future refinement.

Contents

Abstract	iii
1. Theory	3
1.1. Positron Physics	3
1.2. Positron Sources and Beams	3
1.2.1. Pair Production	3
1.2.2. β^+ Decay	4
1.3. Interaction of Positrons with Matter	4
1.3.1. Thermalization	4
1.3.2. Diffusion	5
1.3.3. Reemission	6
1.3.4. Epithermal Positron Emission	6
1.3.5. The Positron Work Function	7
1.4. Positron Moderation	7
1.4.1. Moderator Materials	8
1.4.2. Moderator Geometries	9
1.4.3. Moderation Reemission Yield	10
1.4.4. Brightness Enhancement and Remoderation	11
1.4.5. Moderated Positron Beam Characteristics	12
2. Setup for Low-Energy Positron Experiments at TUM	15
2.0.1. Beam Creation	15
2.0.2. Beam Guidance and Transport	16
2.0.3. Sample Chamber and Holder	17
2.0.4. Detection and Data Acquisition	19
3. Development of an Active Sampleholder with On-Board Voltage Control	21
3.1. Design	21
3.2. DC-DC Charge Pump	21
3.3. ADC readout	23
3.4. Open-Loop System Characterization	23
3.4.1. Response time	23
3.4.2. Reproducibility	24
3.4.3. Long-Term Stability	25
3.4.4. Dependence on Illumination Power	25
3.4.5. PWM Duty Cycle to Output Voltage Mapping	26

3.5. PID Control Loop	27
4. Beam Optimization	31
4.1. Magnetic Coil optimization	31
4.2. Lens Voltage Optimization	34
5. Investigation of the Energy Spectrum and Yield of Positrons after Remoderation	37
5.1. Measurement Procedures	37
5.1.1. Reemission Spectrum Measurement	37
5.1.2. Reemission Yield Measurement	37
5.2. Tungsten	38
5.2.1. Reemission Spectrum	38
5.2.2. Reemission Yield	41
5.3. Nickel	43
5.3.1. Reemission Spectrum	43
5.3.2. Reemission Yield	44
5.4. Platinum	46
5.4.1. Reemission Spectrum	46
5.5. Background	47
5.5.1. Reemission Spectrum	47
5.5.2. Reemission Yield	49
6. Discussion and Outlook	51
Acknowledgments	55
Appendices	57
A. Experimental Setup	59
B. Reemission Yield Estimation	61
Acronyms	62
List of Figures	65
Bibliography	69

Introduction

Positrons, as the antimatter counterparts of electrons, provide unique capabilities for probing fundamental properties of materials such as defect distributions or chemical compositions in a non-destructive way. Applications in surface science and depth-resolved defect studies, such as Positron Annihilation Spectroscopy (PAS), rely on the ability to precisely control the implantation energy of positrons. However, common positron sources, whether from radioactive isotopes like ^{22}Na or from pair production, produce positrons with a broad energy spectrum, extending up to hundreds of keV or even MeV. Such a wide energy distribution is unsuitable for many PAS experiments.

To overcome this limitation, a process known as positron moderation is used. This technique transforms the initial high-energy, polychromatic beam into a low-energy, quasi-monoenergetic beam. This is achieved by implanting the primary positrons into a material called a moderator. In it, the positrons thermalize, and a fraction of them can diffuse back to the surface and be reemitted with a narrow energy distribution determined by the moderator's negative positron work function. The shape and energy of this reemitted spectrum are fundamental properties that determine the quality and performance of the resulting positron beam.

The goal of this thesis is the development and implementation of a new experimental apparatus to measure the energy spectrum of these remoderated positrons. For this purpose, a Retarding Field Analyzer (RFA) was designed and integrated into the existing Setup for Low-Energy Positron Experiments (SLOPE) at TUM. A central component of this work was the construction of a galvanically isolated active sampleholder. This device utilizes an on-board, PID-controlled DC-DC charge pump to provide stable and precise voltage biasing for the retarding grid, operating independently from the main beamline potentials.

The new setup was then characterized, and the positron beam optics were optimized for the new configuration. Finally, the functionality and limitations of the setup were demonstrated through a series of measurements on tungsten, nickel, and platinum samples, attempting to determine both their reemission spectra and energy-dependent reemission yields.

1. Theory

The positron was first postulated by Dirac in 1930 as a consequence of the Dirac equation, which describes relativistic electrons [1]. This equation yielded solutions with both positive and negative energy states. To account for the negative energy solutions, Dirac proposed the existence of a new particle, an "anti-electron," which would have the same mass as an electron but an opposite electric charge. Two years later, Anderson detected the positron in a cloud chamber while studying cosmic radiation, confirming Dirac's prediction [2].

1.1. Positron Physics

The positron is the antiparticle of the electron, with identical mass ($511 \text{ keV}/c^2$) and spin ($\frac{1}{2}$), but opposite electric charge and magnetic moment. While stable in a vacuum, positrons rapidly thermalize within a few picoseconds after entering a solid, followed by diffusion through the material until they annihilate with electrons. In PAS, the resulting annihilation radiation is analyzed to extract information about the local electron density and momentum distribution in the solid [3].

1.2. Positron Sources and Beams

In general, two methods are used to obtain positrons: pair production, typically used in large-scale accelerator facilities, and β^+ decay from radioactive isotopes, common in laboratory-scale experiments.

1.2.1. Pair Production

Pair production is the materialization of a positron-electron pair from a high-energy photon. For this process to occur, the photon's energy must exceed the combined rest mass of the two particles, $2m_e c^2 \approx 1.022 \text{ MeV}$. To conserve momentum, the interaction must take place in the presence of a third body, typically an atomic nucleus. The process can be described as:

$$\gamma \rightarrow e^+ + e^- \text{ (in the presence of a nucleus)} \quad (1.1)$$

[4]. Electron linear accelerators (**linacs**) can be used to generate intense positron beams via this method. A high-energy electron beam strikes a beam dump, producing high-energy bremsstrahlung photons. These photons are then used for pair production

1. Theory

within the same or possibly another material, creating a large flux of positrons. An alternative approach is employed at nuclear reactor-based facilities like the NEutron induced POsitron source MUUniCh (NEPOMUC), which uses high-energy gamma rays released from thermal neutron capture in Cadmium-113 to induce pair production in platinum foils. [5]

1.2.2. β^+ Decay

During β^+ decay, a proton within an unstable, proton-rich nucleus is transformed into a neutron, emitting a positron (e^+) and an electron neutrino (ν_e). The positron carries away some of the energy released in the decay. Since it is a three-body process, the energy spectrum of the emitted positrons is continuous, ranging from zero up to a maximum energy that depends on the specific nuclear transition. The most commonly used isotope for laboratory positron sources is Sodium-22 (^{22}Na), which decays with a half-life of about 2.6 years and has a positron endpoint energy of 545 keV. The predominant decay channel of ^{22}Na is [6]:



1.3. Interaction of Positrons with Matter

When a positron enters a solid, it rapidly loses energy through a sequence of processes until it reaches thermal equilibrium with the host lattice, where it diffuses until it annihilates. This process can be divided into two stages: thermalization and diffusion.

1.3.1. Thermalization

Upon entering a material, a high-energy positron loses its energy primarily through inelastic collisions with electrons, leading to ionization and excitation of the lattice atoms. At lower energies (below a few hundred eV), energy loss through plasmon (only in metals) and ionization becomes dominant. Finally, at near-thermal energies, the primary energy loss mechanism is through interaction with phonons. This slowing-down process, known as thermalization, is very rapid, happening within a few picoseconds. [7]

The resulting implantation depth distribution for positrons implanted at a specific energy can be described with Makhovian profiles:

$$p(z) = \frac{mz^{m-1}}{z_0^m} \exp \left[-\left(\frac{z}{z_0} \right)^m \right] \quad (1.3)$$

with

$$z_0 = \frac{A}{\rho \Gamma(1 + \frac{1}{m})} E^n \quad (1.4)$$

where $p(z)$ is the probability of a positron stopping at a depth z . The parameters m , n and A are material-specific Makhov parameters, ρ is the density of the material and E

is the implantation energy in keV. From the Makhovian profile, the average stopping depth can be calculated as [8]:

$$\bar{z} = \frac{z_0}{\Gamma(1 + \frac{1}{m})} = \frac{A}{\rho} E^n . \quad (1.5)$$

Figure 1.1 shows the Makhovian profiles for positrons in Tungsten and Nickel at various implantation energies.

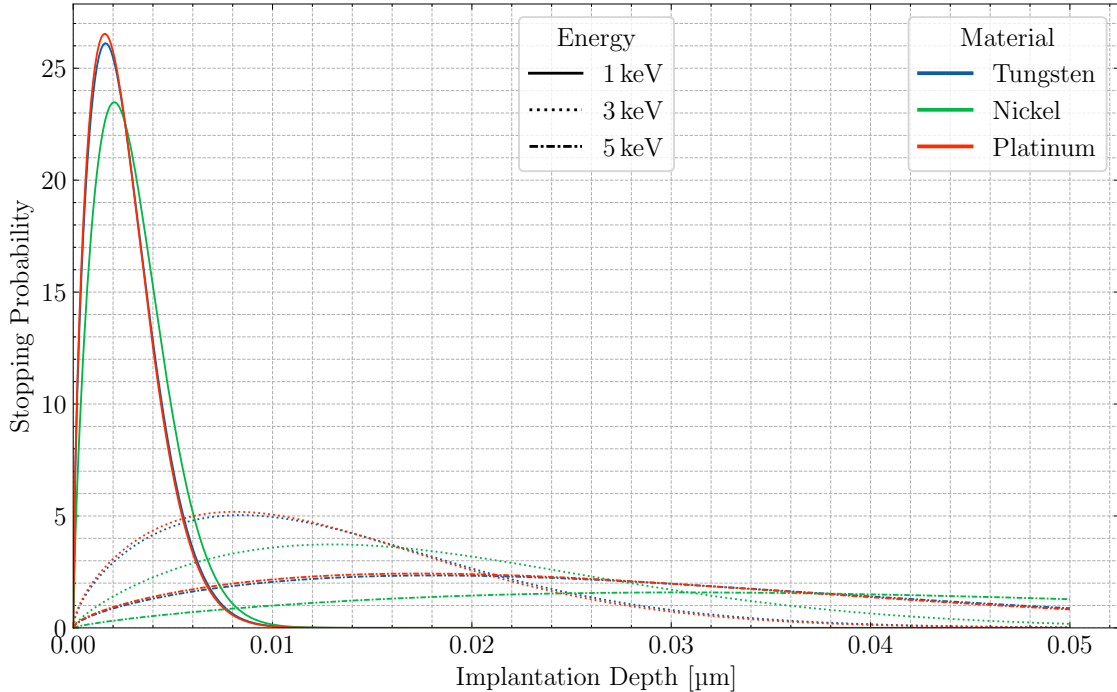


Figure 1.1.: Makhovian profiles for positrons in Tungsten, Nickel and Platinum at various implantation energies. The parameters used for the Makhovian profiles are taken from [8].

1.3.2. Diffusion

After thermalization, the positron exists in a delocalized Bloch state and undergoes random, diffusive motion through the crystal lattice. It continues this motion for its remaining lifetime ($\tau_b \approx 100\text{ps}$ in metals) before annihilating. The average distance a positron travels during this phase is its diffusion length, L_+ , which is typically in the order of 100 nm in a defect-free crystal. During this time, the positron effectively probes the local electronic environment of the material. If it encounters an open-volume defect, such as a vacancy or a dislocation, the missing positive ion core creates an attractive potential well, which can trap the positron until it annihilates. Using PAS, the resulting differences in the annihilation signal can be used to characterize the defect type, size

1. Theory

and concentration. This includes measuring the increased positron lifetime due to lower electron density in the defect with Positron Annihilation Lifetime Spectroscopy (PALS), but also changes in the electron momentum signature measured by Doppler Broadening Spectroscopy (DBS) and Angular Correlation of Annihilation Radiation (ACAR), as a defect-trapped positron is more likely to annihilate with low-momentum valence electrons. [9, 3]

1.3.3. Reemission

During diffusion, a positron can reach the surface of the material again before annihilating. In a homogeneous material, the probability of such back diffusion is given by:

$$J(E) = \int_0^{\infty} \exp\left(-\frac{z}{L_+}\right) p(z, E) dz \quad (1.6)$$

where L_+ is the positron diffusion length, E is the implantation energy and $p(z, E)$ is the Makhovian stopping profile. Once at the surface, several processes can occur depending on the surface conditions and electronic properties of the material. The positron can capture an electron from the surface and form a positronium atom (a bound state of an electron and a positron), which is then emitted into the vacuum. It can also become trapped in an image-potential-induced potential well at the surface, where it remains until it annihilates with an electron from the material. The third possibility, which is the primary focus of the experimental work in this thesis, is the reemission of the positron as a free particle. If the positrons are not fully thermalized when reaching the surface, they are called epithermal; if they have thermalized, they are called slow positrons. The energy distribution of slow positrons is described by the positron work function. [10]

1.3.4. Epithermal Positron Emission

In addition to the reemission of fully thermalized positrons, a fraction of positrons can diffuse back to the surface before reaching thermal equilibrium with the lattice. These are known as epithermal positrons. This process is particularly significant at low implantation energies, where positrons are stopped very close to the surface, increasing the probability of them reaching the surface before losing all their excess kinetic energy [11].

Unlike thermalized positrons, which are reemitted with a narrow kinetic energy distribution determined by the positron work function ϕ_+ , epithermal positrons are emitted with a broader energy spectrum that extends to higher energies. While the thermal reemission process is governed by the positron's diffusion length L_+ , the contribution of epithermal positrons can be modeled by considering a much shorter characteristic length, often referred to as the epithermal scattering length, l_+ . This length represents the mean free path of a hot positron in the material. The probability of epithermal emission can be calculated using a similar formalism as for thermal reemission (Equation

1.6), but by substituting the thermal diffusion length L_+ with the epithermal scattering length l_+ . As will be shown, this epithermal component can account for a significant portion of the total reemission yield at low incident energies [11].

1.3.5. The Positron Work Function

The positron work function, ϕ_+ , defines the energy required to move a thermalized positron from the bulk of a material to the vacuum level just outside its surface. To understand this quantity, it can be compared to the well-known electron work function, ϕ_- . Both work functions are composed of a bulk chemical potential (μ) and a surface electrostatic dipole barrier (Δ). The work functions for an electron (ϕ_-) and a positron (ϕ_+) can be expressed as:

$$\begin{aligned}\phi_- &= \Delta - \mu_- \\ \phi_+ &= -\Delta - \mu_+\end{aligned}\tag{1.7}$$

[10]. So the difference lies in the chemical potential and the sign of the surface dipole term, Δ . The dipole barrier is primarily caused by the tailing of the electron distribution into the vacuum. While this potential opposes the escape of an electron, it is attractive to a positron, which is repelled by the ion cores within the bulk. This inversion of the dipole's effect results in the $-\Delta$ term in the expression for ϕ_+ and is the reason why the positron work function can be negative for some materials (e.g. W and Ni), while the electron work function is always positive [3]. Figure 1.2 shows a schematic representation of these potentials.

For materials with a negative positron work function ($\phi_+ < 0$), the spontaneous emission of a thermalized positron from the surface becomes an energetically favorable process. The reemitted slow positron emerges with a well-defined kinetic energy equal to the magnitude of the work function, $E_{kin} = |\phi_+|$, with a small thermal spread given by the sample temperature. This process is the fundamental principle behind positron moderators, which utilize materials with a large negative work function to efficiently produce the monoenergetic slow positron beams required for many surface-sensitive experiments. [10]

1.4. Positron Moderation

Positrons produced from radioactive sources or pair production typically have a broad, continuous energy spectrum, extending up to several hundred keV or even MeV. For most experimental applications, particularly those involving surface science and depth-profiling, such a beam can not be used. A well-defined, monoenergetic positron beam is required to precisely control the implantation depth and to perform high-resolution spectroscopic measurements. The process of turning the initial high-energy, broad-distribution beam into a monoenergetic, low-energy beam is known as positron moderation. This is achieved by directing the primary positrons into a moderator, which relies

1. Theory

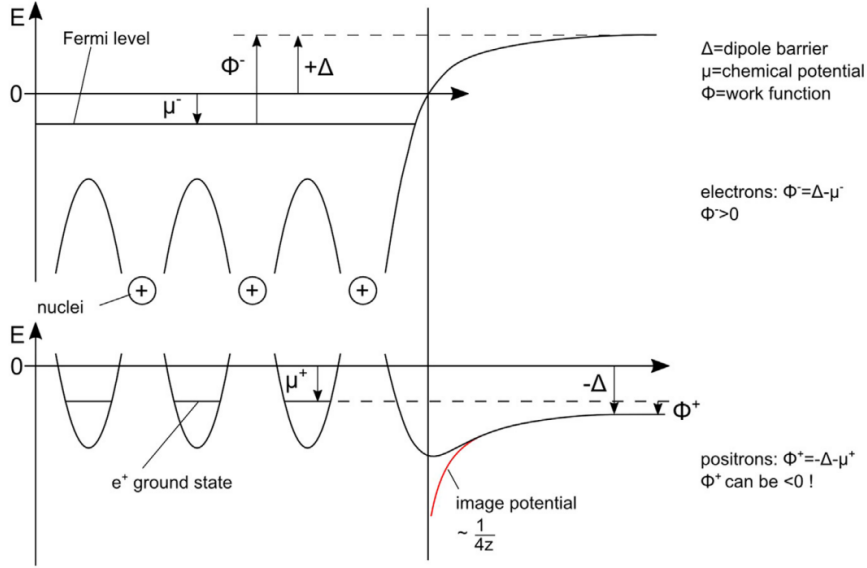


Figure 1.2.: Schematic of the potential energy for an electron (top) and a positron (bottom) at a metal-vacuum interface [10]. The diagram illustrates the bulk chemical potentials (μ_- and μ_+), the surface dipole barrier (Δ), and the resulting work functions (ϕ_- and ϕ_+). The negative work function for the positron ($\phi_+ < 0$) leads to its spontaneous emission from the surface.

on the negative positron work function to reemit thermalized positrons into the vacuum with a small, well-defined kinetic energy. Although the efficiency of this process is low, the resulting concentration of positrons into a narrow energy window increases the beam's phase space density, or brightness, which is essential for most PAS experiments. The effect of this transformation is illustrated in Figure 1.3. [10]

1.4.1. Moderator Materials

The essential characteristic of an effective positron moderator is a negative positron work function ($\phi_+ < 0$), which makes the spontaneous reemission of thermalized positrons from the surface an energetically favorable process. Additionally, a high-quality moderator should possess a long positron diffusion length (L_+) to maximize the probability that positrons thermalized deep within the material can reach the surface before annihilating. This requirement favors single-crystalline materials with a low density of defects and impurities.

Solid-state moderators are the most widely used type. Well-annealed, single-crystal metals such as Tungsten (W) and Nickel (Ni) are common choices due to their negative work functions and structural properties. Tungsten (W) is one of the most widely used and efficient moderator materials, particularly in its (100) and (110) crystallographic

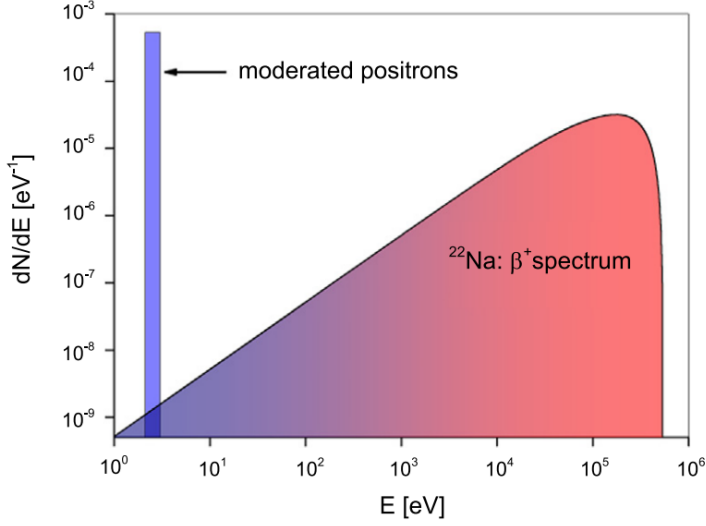


Figure 1.3.: β^+ spectrum of ^{22}Na before and after moderation. Figure taken from Hugenschmidt 2016 [10]

orientations, due to its high density, long diffusion length, and high negative work function ($\phi_+ \approx -3.0$ eV). The preparation of these moderators is also very important. Surfaces must be clean and free of defects, as contaminants or structural imperfections can trap positrons, drastically reducing the reemission yield and smearing the reemission spectrum [12]. While solid moderators are the focus of this thesis, it is worth noting that other types exist. For instance, solid rare-gas moderators, such as frozen neon or argon, which achieve higher moderation efficiencies (though still typically <1%) via the emission of epithermal positrons. However, they produce a less monoenergetic beam than metallic moderators and require complex cryogenic systems to be maintained [13, 10].

1.4.2. Moderator Geometries

The physical arrangement of the positron source and the moderator can be configured in two general geometries: reflection and transmission.

In **reflection geometry**, also known as back-reemission, the positron source and the extracted slow positron beam are situated on the same side of a thick moderator crystal. High-energy positrons are implanted into the moderator, thermalize, and a fraction of them diffuse back to the incident surface, where they are reemitted. While simple to implement, this geometry suffers from a significant drawback known as the "source-shadow" problem when used as a primary moderator. The physical presence of the source and its holder can obstruct the path of the reemitted slow positrons, recapturing a portion of them and thereby reducing the effective beam intensity and quality [12].

1. Theory

The **transmission geometry** was developed to overcome this limitation. In this configuration, the moderator is a thin, self-supporting film, typically a few hundred to a few thousand angstroms thick. The high-energy positron source is placed on one side of the film, and the reemitted slow positrons are extracted from the opposite side. This arrangement spatially separates the primary source from the moderated beam, completely eliminating the source-shadow problem and allowing for more efficient beam transport. The challenge in this geometry is the fabrication of high-quality, single-crystal thin films that are robust enough to be self-supporting. The film's thickness must be optimized to be thick enough to stop a significant fraction of the incident high-energy positrons but thin enough to allow them to diffuse across and reach the opposite surface before they annihilate. Chen et al. demonstrated the viability of this approach using epitaxial single-crystal W(100) films, achieving high reemission yields and establishing transmission moderators for advanced positron beamlines [12].

1.4.3. Moderation Reemission Yield

The efficiency of a moderator is quantified by its reemission yield, Y , defined as the number of slow positrons emitted per incident high-energy positron. For primary moderation of positrons from a source, this value is typically low, in the range of 10^{-4} to 10^{-3} [10]. The theoretical yield depends on the implantation profile of the primary positrons, the positron diffusion length in the moderator, the moderator thickness, and the branching ratio for reemission at the surface. For a thin film of thickness T , the yields for back-reemission (Y_B) and forward-reemission (Y_F) can be calculated by integrating the product of the positron stopping profile, $p(x)$, and the probability that a positron at depth x will diffuse to the surface. This probability is described by a Green's function, leading to the expressions:

$$Y_B(E) = B \int_0^T \frac{\sinh((T-x)/L_+)}{\sinh(T/L_+)} p(x, E) dx \quad (1.8)$$

$$Y_F(E) = B \int_0^T \frac{\sinh(x/L_+)}{\sinh(T/L_+)} p(x, E) dx \quad (1.9)$$

[12] where B is the branching ratio for slow positron reemission at the surface, L_+ is the positron diffusion length, and $p(x, E)$ is the Makhovian stopping profile for an incident energy E .

These equations show that the yield is strongly dependent on the incident positron energy. For a transmission moderator, at low energies, most positrons stop near the entrance surface and either annihilate or are reemitted backward, resulting in a low forward yield. As the energy increases, the implantation profile shifts deeper into the film, closer to the exit surface, causing the forward yield Y_F to increase. However, if the energy becomes too high, a significant fraction of positrons will pass through the film without thermalizing or will be implanted too deep to diffuse out, causing the yield to decrease again. Consequently, for any given film thickness, there exists an

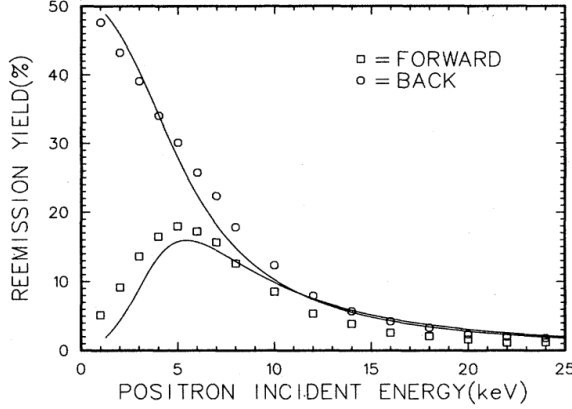


Figure 1.4.: Forward and backward reemission yield as a function of incident positron energy for a 1000 Å thick W(100) film. The forward yield (labeled with squares) peaks at an optimal energy, while the backward yield (labeled with circles) decreases monotonically. Figure adapted from Chen et al. [12]

optimal incident energy that maximizes the forward-reemission yield. This characteristic behavior can be seen in Figure 1.4, which plots the measured forward and backward reemission yields for a 1000 Å W(100) film as a function of incident positron energy [12]. The forward yield can be seen to peak, while the backward yield monotonically decreases as the positrons are implanted deeper into the material and further away from the entrance surface. In this specific case, Chen et al. measured a maximum forward-reemission yield of 18% at an optimal incident energy of 5 keV. For a thicker 2500 Å film, the optimal energy shifted to 10 keV with a corresponding maximum yield of 12% [12].

1.4.4. Brightness Enhancement and Remoderation

While primary moderation successfully transforms a high-energy, polychromatic positron source into a low-energy, quasi-monoenergetic beam, the resulting beam brightness is often insufficient for demanding applications such as positron microscopy, micro-diffraction, or spatially resolved defect studies [6]. Brightness, a figure of merit for beam quality, is defined as:

$$B = \frac{I}{\theta^2 d^2 E} \quad (1.10)$$

where I is the beam intensity, d is its diameter, θ is its angular divergence, and E is its energy [3]. For a beam guided by electrostatic or magnetic lenses (which exert conservative forces), Liouville's theorem dictates that the phase-space volume occupied by the beam remains constant. Consequently, reducing the beam diameter (d) inevitably leads to an increase in its angular divergence (θ), leaving the overall brightness unchanged.

1. Theory

To overcome this fundamental limitation, a technique known as remoderation is employed. This process exploits the fact that moderation is a non-conservative process. The procedure involves taking a moderated positron beam, accelerating it to a few keV, and focusing it onto a second moderator, known as a remoderator. Inside the remoderator, the positrons thermalize, losing the large angular momentum they acquired during focusing. The result is a new beam with a significantly smaller diameter but without the corresponding increase in angular divergence, leading to an increase in brightness [3].

This concept is illustrated in Figure 1.5. The diagonal lines represent the effect of focusing, where the beam area is traded for angular divergence at constant brightness. The horizontal lines represent the remoderation step, which reduces the beam area at a constant (low) angular divergence, thereby moving the beam to a state of higher brightness.

This gain in brightness comes at the cost of beam intensity, as the reemission efficiency of each remoderation stage is typically in the range of 20-30% [6]. However, the brightness can be increased by 100 to 500 times [3]. The process can be repeated in multiple stages, though the cumulative loss in intensity typically limits practical systems to two or three remoderation stages. Furthermore, the positron diffusion length within the remoderator material sets a natural limit on the minimum achievable spot size. Remoderation can be performed in either reflection or transmission geometry, with the latter being advantageous for separating the primary and remoderated beams in multi-stage systems [6].

1.4.5. Moderated Positron Beam Characteristics

A moderated positron beam is characterized by its narrow energy and angular distributions, which are primarily governed by thermal effects. The kinetic energy of the reemitted positrons shows a peak at a value equal to the magnitude of the negative positron work function, $E_{kin} = |\phi_+|$. This peak is not a perfect delta function but has an inherent energy spread due to the thermal motion of the positrons within the moderator lattice just before emission. In practice, the observed energy distribution can be further broadened by several effects, including the emission of inelastically scattered or epithermal positrons, surface roughness, and local variations in the surface dipole potential caused by adsorbates [10]. Nevertheless, high-resolution measurements by Fischer et al. confirmed that the core energy distribution of elastically reemitted positrons is well-described by a Maxwell-Boltzmann distribution, which for positron emission normal to the surface is given by [14]:

$$F(E) \propto E \exp(-E/k_B T) \quad (1.11)$$

where E is the kinetic energy relative to the peak, k_B is the Boltzmann constant, and T is the temperature of the moderator. At room temperature (300 K), this thermal broadening results in a full width at half maximum (FWHM) of approximately 75 meV. [14]

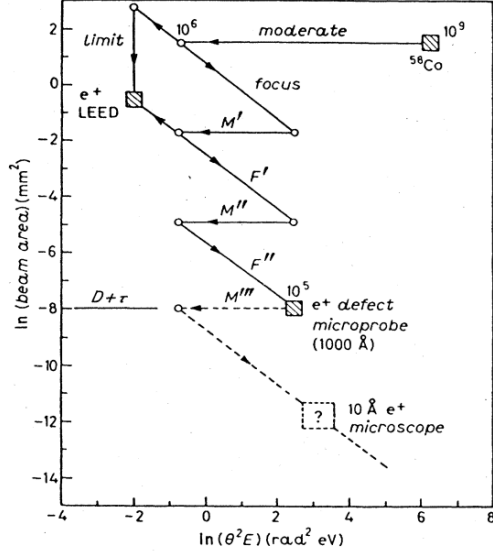


Figure 1.5.: Focusing the beam (diagonal lines) conserves brightness by trading beam area for angular divergence. Remoderation (horizontal lines) is a non-conservative process that creates a smaller effective source size while restoring low angular divergence, thus increasing brightness.. Figure from Schultz and Lynn [3].

Similarly, the angular distribution of the reemitted positrons is strongly peaked in the direction normal to the surface. The small spread in the emission angle is also a consequence of the thermal motion of the positrons parallel to the surface. Fischer et al. showed that the measured angular widths are consistent with predictions based on a thermal distribution, with a typical FWHM of $10^\circ\text{--}25^\circ$ at room temperature, depending on the material's work function. Both the energy and angular spreads can be significantly reduced by cooling the moderator to cryogenic temperatures. [14].

2. Setup for Low-Energy Positron Experiments at TUM

The experimental work in this thesis was conducted at the Setup for Low-Energy Positron Experiments at TUM. This instrument is a laboratory-scale setup designed to produce a low-energy, monoenergetic positron beam for surface and near-surface studies. The design and original purpose of the setup for positron-induced Auger electron spectroscopy are detailed in the dissertation of Straßer [4]. The system has since been recommissioned and upgraded for Doppler-broadening spectroscopy, with its modern configuration described in the theses of Mathes and Suhr [15, 16]. A schematic of the current setup is shown in Figure 2.1.

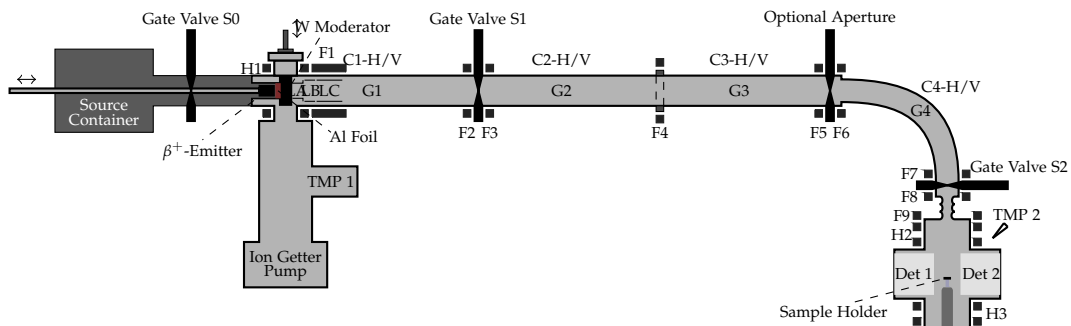


Figure 2.1.: Schematic drawing of the Labbeam with designations of coils and valves.
Figure taken from Springl 2023 [17]

2.0.1. Beam Creation

The Labbeam utilizes a ^{22}Na radioactive source, as described in Section 1.2, with an activity of approximately 855 MBq (as of August 2025). The source is encapsulated and mounted on a movable rod, allowing it to be positioned directly behind the moderator or retracted into a shielded lead enclosure for safety. The source container is maintained at a pre-vacuum pressure and is separated from the Ultra-High Vacuum (UHV) of the beamline by a 5 μm thick aluminum foil. This foil is thin enough to allow the high-energy positrons to pass through with minimal absorption.

After passing through the foil, the positrons impinge on a 1 μm thick, single-crystal

2. Setup for Low-Energy Positron Experiments at TUM

W(100) transmission moderator. As detailed in Section 1.4, the moderator thermalizes a fraction of the incident positrons, reemitting them from the opposite surface with a narrow energy distribution centered around 3 eV. To extract the slow positrons, the moderator can be biased with a positive voltage (e.g., +30 V) to provide them with an initial kinetic energy for transport. This provides the reemitted slow positrons with an initial longitudinal kinetic energy. A special capability of the SLOPE setup, however, is that it can also operate with a 0 V bias, allowing for the extraction of a slow positron beam. The entire moderator chamber is enclosed in a lead shielding to contain the gamma radiation from the source [16, 15].

2.0.2. Beam Guidance and Transport

The transport of the low-energy positron beam from the moderator to the sample is achieved via magnetic guidance, while electrostatic fields are used for initial and final acceleration. The primary guidance is provided by a longitudinal magnetic field, which confines the positrons to a helical trajectory along the beam axis.

Immediately following the moderator, a set of three cylindrical electrodes is used to homogenize the initial electric field, preventing the defocusing of slightly off-axis positrons [15]. The magnetic guidance begins with a pair of Helmholtz coils surrounding the moderator chamber, generating a field of approximately 25 G. The beamline consists of a straight section followed by a 90° curved section, both of which are wrapped with solenoid coils to create a continuous guiding field. This 90° bend serves two purposes: it acts as an energy filter, allowing only the low-energy moderated positrons to be successfully transported, and it shields the detectors in the sample chamber from the direct line-of-sight of the high-energy gamma radiation from the ^{22}Na source.

To compensate for the Earth's magnetic field and other external fields, a series of extended correction coils is installed along the beamline. These coils generate weak magnetic fields perpendicular to the main guiding field, allowing for precise steering of the beam. Additional Helmholtz-like coils are placed at the junctions between different sections of the apparatus to ensure a smooth transition of the magnetic field [16].

2.0.3. Sample Chamber and Holder

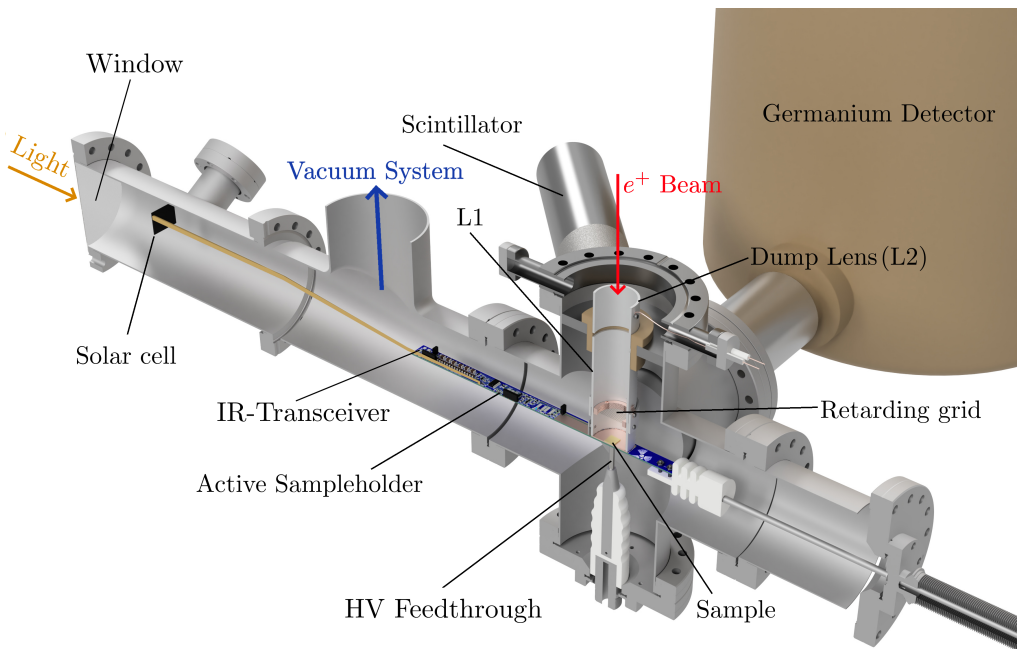


Figure 2.2.: Rendered view of the sample chamber.

The beamline terminates at the sample chamber, which operates under UHV conditions with typical pressures ranging from 10^{-8} to 10^{-7} mbar. As depicted in Figure 2.2, positrons enter into the top of the chamber from the beamline, which delivers an intensity of approximately $8.84 \cdot 10^4$ moderated positrons per second to the sample position [18].

The sample is mounted on the active sampleholder, which is described in detail in Chapter 3. This assembly is mounted to the front of the chamber and supported by a spring-loaded iron pin connected to an external High-Voltage (HV) power supply, enabling the sample to be biased to potentials of up to -40 kV for positron acceleration.

The rear of the chamber is extended by a tube that forms the interface to the UHV pumping system. This section is sealed with a vacuum window, which allows light to pass through to power the solar cell of the active sampleholder and permits command transmission via an Infrared (IR) link.

For this thesis, a new electrostatic lens system was designed and installed to allow for retarding field measurements. The design and optimization of this Retarding Field

2. Setup for Low-Energy Positron Experiments at TUM

Analyzer were performed using COMSOL Multiphysics [19], a finite element analysis software. The goal was to develop a lens configuration that could efficiently guide the incoming positron beam onto the sample with minimal spot broadening, while also collecting and directing reemitted positrons to a well-defined annihilation area on a beam dump, sufficiently distant from the sample to minimize background.

Initial design considerations involving just a simple retarding grid above the sample proved unsuitable. Simulations showed that with the sample holder biased to high potentials, the strong electric field from the surrounding grounded chamber components would "leak" into the region between the sample and the grid. This stray field was found to be significantly larger than the intended retarding potential, making the energy analysis impossible.

To solve this problem, a shielded two-lens design was developed, consisting of two primary electrostatic lenses, L1 and L2. The effectiveness of this configuration was validated through the simulations shown in Figure 2.4.

The first component, the **Retarding Field Lens (L1)**, is a long, cylindrical electrode that acts as a Faraday cage, shielding the positrons from external fields and ensuring that the retarding potential is applied uniformly across the grid. In practice, L1 consists of two separate cylindrical sections that are joined together when the sampleholder is slid into place, which allows for sample changes without dismantling the entire lens assembly. This lens, which has the retarding grid mounted on its inside, is held at the same variable potential as the grid itself via the active sampleholder. This creates a nearly electric-field-free region for the positrons, ensuring that the only significant potential gradient they experience is the one applied by the retarding grid, as shown in the detailed view in Figure 2.3. The axial magnetic field present in the chamber (Figure 2.4b) confines the positrons, causing them to precess along the central axis and preventing them from drifting into the lens walls. As shown in Figure 2.4c, the incoming positron beam is successfully guided through L1 and focused onto the sample with only minimal beam broadening.

The second component, the **Dump Lens (L2)**, is a shorter lens placed above L1. While L1 shields the lower section, the potential from the grounded chamber could still leak into its upper opening, causing a broad annihilation area. To create a sharp and predictable annihilation spot, L2 is held at a more negative potential relative to L1 (up to -6 kV). This creates an attractive potential well that guides positrons overcoming the retarding potential onto a well-defined area on the dump lens, as shown in the particle trajectory simulation in Figure 2.4d. This design also limits the maximum bias potential of the sampleholder to -6 kV, since the beam dump must be held at a more negative potential to function.

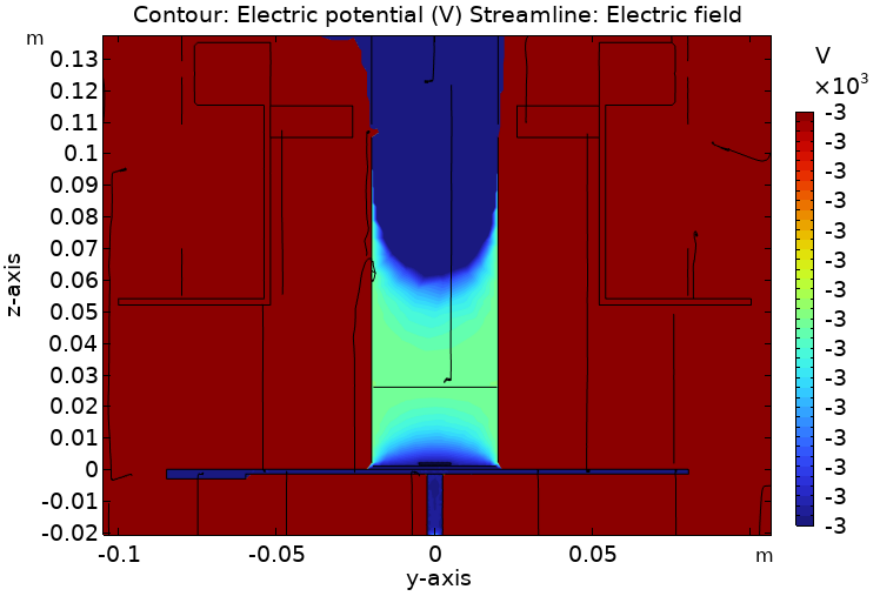


Figure 2.3.: Detailed view of the simulated electric potential in the retarding grid region. A clear retarding field gradient can be seen, allowing only positrons with sufficient kinetic energy to overcome the potential barrier to pass through.

2.0.4. Detection and Data Acquisition

The experimental setup has two detector pairs to characterize annihilation events. The main detectors at SLOPE, used for Doppler-broadening spectroscopy of positrons annihilating within the sample, are two opposing High-Purity Germanium (HPGe) detectors. This configuration allows both single-detector and coincidence measurements of the 511 keV annihilation line. To reduce background and only let radiation from the samples to the detectors, each HPGe detector is housed within a W-Cu alloy shield, providing a narrow line-of-sight focused on the sample position.

For the primary measurement of this work, the determination of the remoderated positron energy spectrum, a second detector pair was installed, consisting of the two BGO scintillation detectors aimed at the upper lens (L2). These detectors count annihilation events from remoderated positrons that have overcome the retarding potential and reached the dump. The reemitted positron spectrum is then produced by recording the coincidence count rate as a function of the applied retarding grid voltage. The signals from both detector pairs are processed by a single CAEN Multi-Channel Analyzer. This unit digitizes the incoming signals and records a list of events, each consisting of a timestamp and energy value. This data is then processed to construct the required energy spectra and to determine coincidence event rates [16].

2. Setup for Low-Energy Positron Experiments at TUM

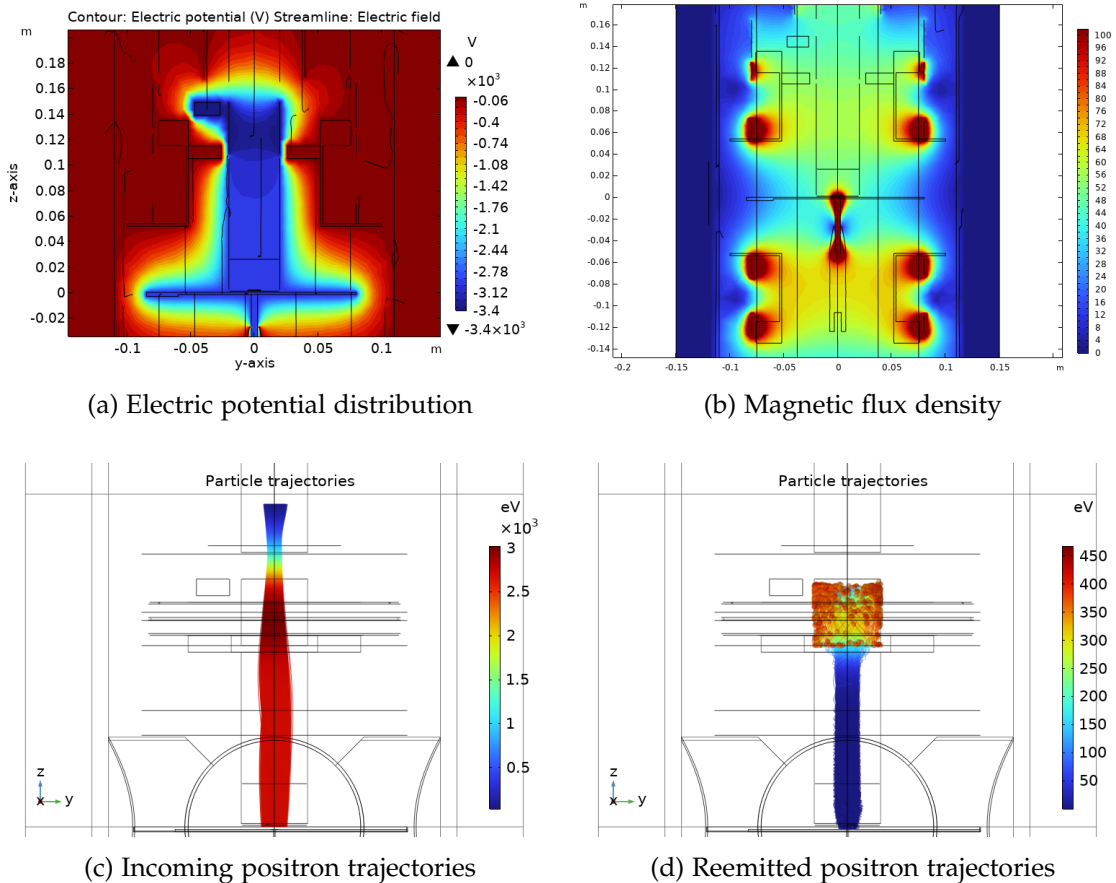


Figure 2.4.: COMSOL Multiphysics simulations of the sample chamber. (a) The electric potential with the sample at -3000 V, the retarding lens (L1) at +3 V (relative to the sampleholder), and the dump lens (L2) at -3600 V. (b) The magnitude of the magnetic flux density generated by external coils, which confines the beam. (c) Trajectories of the incoming positron beam focused onto the sample. (d) Trajectories of reemitted positrons that overcome the retarding potential, showing their precession and annihilation on the dump lens.

3. Development of an Active Sampleholder with On-Board Voltage Control

To perform retarding grid measurements, a galvanically isolated device capable of generating a precise potential on the sample was required. Building upon a previous design by Brenner [20], a new active sampleholder was developed and implemented. The final design utilizes a closed-loop Proportional-Integral-Derivative (PID) control system (see Section 3.5) to regulate an on-board DC-DC charge pump. This system achieves a stable output voltage in the range of 0 V to 7.8 V with a final accuracy of $\pm 5\text{ mV}$. The following sections detail the design of the hardware and the open-loop characterization, which demonstrated the necessity of a closed-loop control strategy for achieving the required precision and stability.

3.1. Design

The active sampleholder, a 2 cm x 29 cm printed circuit made out of FR4, is powered by an onboard solar cell, which receives light through a window in the chamber. Communication with the sample holder is achieved wirelessly via an IR link. An external control board, connected to a host computer via USB, drives an IR transmitter. On the sample holder, an onboard Microcontroller Unit (MCU) (PIC24FJ32GB002) receives and processes the transmitted commands. A communication protocol was established that allows for setting operational parameters, such as the Pulse-Width Modulation (PWM) duty cycle for the voltage generation, and for retrieving measured data, such as the measured output voltage.

While the communication protocol and general electrical design were adapted from the work of Brenner [20], where vacuum and radiation tolerance were validated, the main modifications for this thesis include a new mechanical form factor and the integration of a new, more efficient DC-DC charge pump.

3.2. DC-DC Charge Pump

The new design uses a custom DC-DC charge pump that is directly controlled by the MCU on the sample holder. This approach is more power efficient and allows for more control over the voltage output. Figure 3.1 shows the schematic of the charge pump. The circuit operates by switching the NPN transistor Q1, which pulls the node between

3. Development of an Active Sampleholder with On-Board Voltage Control

L1 and D8 to ground during its on-time. This allows energy to build up in the inductors L1 and L2. When Q1 turns off, the stored energy is transferred through the diode D8 to the output. C25 and R17 provide decoupling and limit inrush current. The capacitors C26 and C28, together with resistors R19 and R21, form a low-pass filter that smooths the output voltage, which is then monitored via the ADC2 pin. The resistor R13 forms a voltage divider together with R21, to scale down the output voltage to the 2.5 V range of the Analog-to-Digital Converter (ADC) integrated in the MCU. The additional filter stage (R22, C29) suppresses high-frequency voltage spikes that can be generated during the switching of the transistor.

The component values for the output filter were tuned to provide a smooth, low-ripple output voltage while also having a reasonably fast response time to new voltage setpoints.

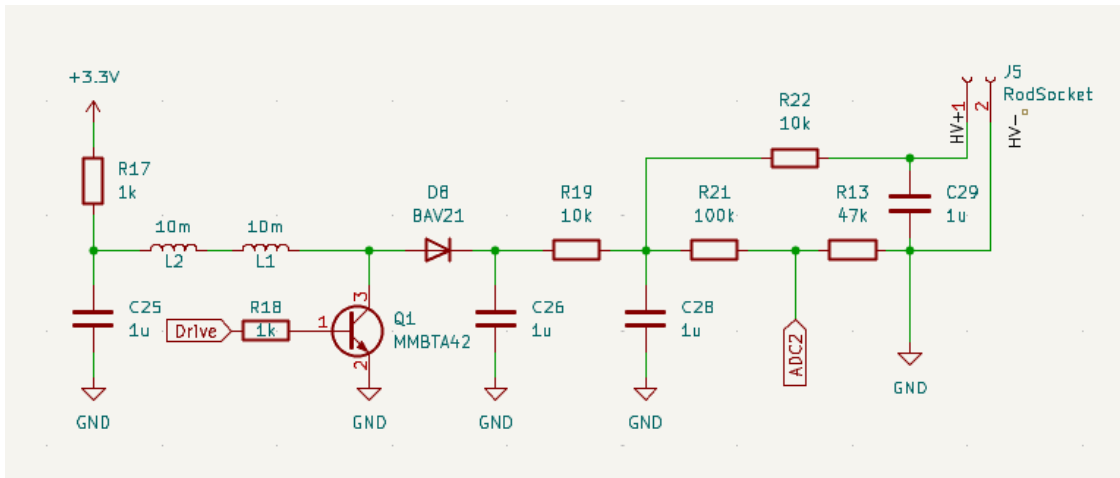


Figure 3.1.: Schematic of the custom DC-DC charge pump. A PWM signal ("Drive") from the MCU switches the transistor (Q1), allowing energy to be stored in the inductors (L1, L2) during its on-state. When Q1 switches off, the stored energy is transferred through the diode (D8) to a low-pass filter stage (C26, C28, R19, R21), which generates a smooth DC output voltage. This output is then scaled down by a voltage divider (R13, R21) and monitored at the "ADC2" pin, providing the necessary feedback for the control system.

3.3. ADC readout

The Analog-to-Digital Converter (ADC) readout is performed using the internal 10 bit ADC of the Peripheral Interface Controller (PIC). However, the communication protocol of the active sampleholder allows for a 16 bit value to be transmitted, allowing 64 samples to be added, which effectively increases the precision to 13 bits. The voltage resolution depends on the voltage divider used to scale the output voltage of the charge pump. The ADC is configured to use the output of a 2.5 V Zener diode as a reference voltage. Using the ratio of the voltage divider (100 k Ω and 47 k Ω), the output voltage V_{out} is calculated from the ADC input voltage V_{in}

$$V_{\text{out}} = V_{\text{in}} \cdot \left(1 + \frac{100 \Omega}{47 \Omega}\right) \approx V_{\text{in}} \cdot 3.13 . \quad (3.1)$$

With 13 bit precision, the ADC has $2^{13} = 8192$ levels. Each ADC step corresponds to

$$\Delta V_{\text{in}} = \frac{2.5 \text{ V}}{8192} \approx 0.305 \text{ mV} . \quad (3.2)$$

Taking the voltage divider into account, the output voltage resolution becomes:

$$\Delta V_{\text{out}} = 0.305 \text{ mV} \cdot 3.13 \approx 0.955 \text{ mV} . \quad (3.3)$$

This means the ADC can detect changes in the charge pump output voltage with a resolution of roughly 1 mV. This resolution can be increased by either averaging more samples, which would require a rework of the communication protocol to allow for larger data packets or by using a higher voltage divider ratio. However latter would reduce the maximum measurable voltage. The current configuration was selected to allow the highest possible resolution while still covering the expected work function voltages.

3.4. Open-Loop System Characterization

Since the charge pump was a new design, it had to be characterised in order to accurately control it. The following properties were measured.

3.4.1. Response time

The system's response to new voltage setpoints was measured to determine its settling time. Figure 3.2 shows the system's response to various voltage changes. To determine the worst-case settling time, the test included large and small voltage steps in both increasing and decreasing directions, covering all possible transitions between the three voltage levels 0.4 V, 3.91 V, and 7.82 V. The results demonstrate that for all tested transitions, the output voltage settles to within 1% of the target value in under 2 seconds. In Figure 3.2, the time $t = 0$ corresponds to the moment the new control signal is sent;

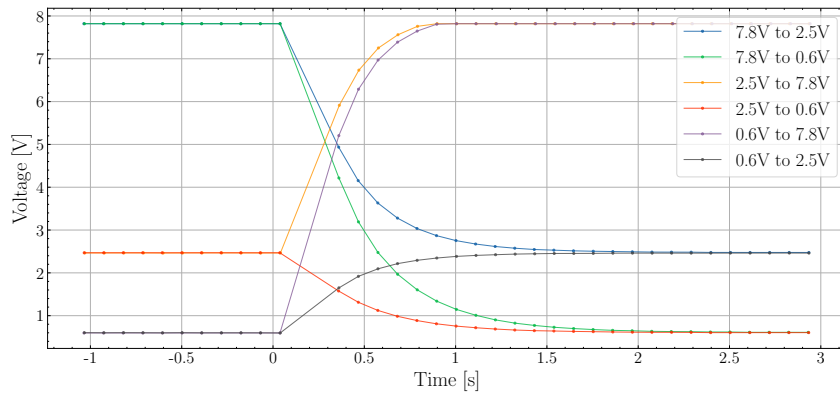


Figure 3.2.: Step response of the DC-DC charge pump for various voltage transitions. The system settles to within 1% of the target value in under 2 s for all transitions.

the initial delay of ~ 50 ms before the voltage changes is due to communication and processing latency. The settling times for these transitions are summarized in Table 3.1. Based on the worst-case result, a 2 s delay was implemented in the control software between setting a new voltage and initiating a measurement, ensuring that the voltage at the sample is stable.

Table 3.1.: Measured settling times to within 1% of the target voltage for various transitions.

Voltage Transition	Settling Time (ms)
7.8 V to 2.5 V	1646
7.8 V to 0.6 V	1860
2.5 V to 7.8 V	899
2.5 V to 0.6 V	1968
0.6 V to 7.8 V	897
0.6 V to 2.5 V	1433

3.4.2. Reproducibility

The reliability with which the system produces the same voltage given the same control input was assessed. The measurement consisted of repeatedly turning the charge pump off (no PWM signal) and setting a fixed PWM duty cycle and measuring the resulting output voltage after 20 seconds. This process was repeated 10 times to get statistical data on the reproducibility. Table 3.2 summarizes the results for various PWM settings. Across different target voltages, the standard deviation of the measured output voltage was consistently low, ranging from 1.3 mV to 2.4 mV. This variation in the order of only a few millivolts confirms that the control authority of the charge pump is stable enough

for the intended application.

Table 3.2.: Reproducibility of the DC-DC Charge Pump Output Voltage. The table presents the mean, minimum, maximum, and standard deviation of the output voltage, measured over 10 repetitions, after repeatedly applying specific, fixed PWM high and low tick configurations.

High Ticks	Low Ticks	Mean (V)	Min (V)	Max (V)	Std Dev (V)
2100	6000	6.1278	6.1264	6.1306	0.0014
2500	6000	4.5703	4.5683	4.5723	0.0013
2750	6000	3.6500	3.6481	3.6533	0.0017
3000	6000	2.8104	2.8074	2.8143	0.0024

3.4.3. Long-Term Stability

Beyond short-term reproducibility, the long-term stability is important since one measurement could take up to an hour. To quantify the inherent drift of the charge pump, the output voltage was monitored for two hours with a fixed PWM duty cycle. The results, shown in Figure 3.3, indicate a mean voltage of 6.003 V with a standard deviation of 2.4 mV and a peak-to-peak fluctuation of 13.5 mV over the two-hour period. This fluctuation is likely due to thermal effects and should be taken into account when performing longer measurements.

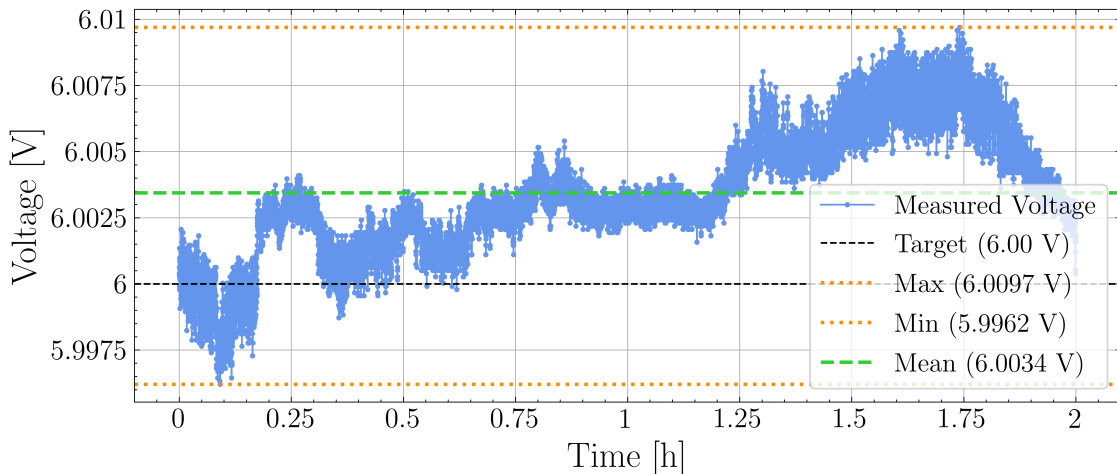


Figure 3.3.: Voltage drift of the chargepump over two hours.

3.4.4. Dependence on Illumination Power

The performance of the active sampleholder is linked to the power supplied by its onboard solar cell. To characterize this dependency, the stability of the charge pump's

output voltage was quantified as a function of the illumination power. For this measurement, a constant PWM duty cycle was maintained while the LED supply current was varied from 0.4 A to 1.5 A. Assuming the LED's power conversion efficiency is constant over this range, the illumination power received by the solar cell is directly proportional to the supply current.

The results, shown in Figure 3.4, demonstrate a direct correlation between the LED current and the charge pump's output voltage, confirming that the output is sensitive to variations in input power. The measurements also revealed specific thresholds. For an LED current below 0.4A, the sampleholder became unresponsive. In the range between 0.4A and 0.8A, the device exhibited unstable behavior, characterized by intermittent communication errors, including dropped data bytes and spontaneous restarts of the onboard microcontroller. Currents above 1.5A weren't measured since this is the maximum rated current for the LED.

To ensure reliable and stable operation, a minimum power level of 1.3A for the illumination LED was selected for all subsequent experiments. The dependence on illumination power demonstrates that an open-loop control strategy, such as using a pre-calibrated lookup table for PWM settings, would be unreliable. Any fluctuation in the light source intensity would directly translate into an unintended change in the output voltage. Therefore, a closed-loop feedback system is required to maintain a precise and stable output voltage, as will be discussed in Section 3.5.

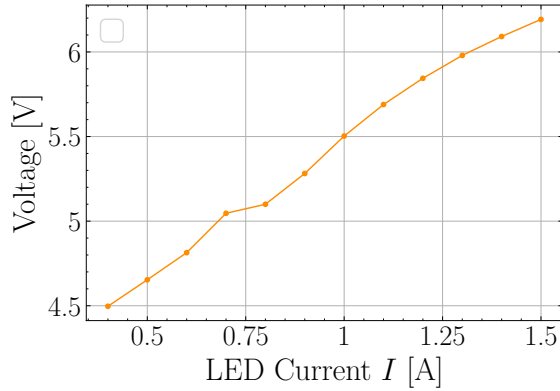


Figure 3.4.: Dependence of the charge pump output voltage on the illumination LED supply current. The measurement was performed with a constant PWM duty cycle to isolate the effect of input power.

3.4.5. PWM Duty Cycle to Output Voltage Mapping

To control the charge pump, it was necessary to characterize the relationship between the PWM control signal and the resulting output voltage. This characterization was

performed by parameterizing the PWM duty cycle in terms of its high and low times. A mapping was then generated by systematically varying the high and low times and recording the corresponding output voltage. The results of this mapping are visualized in the 2D heat map shown in Figure 3.5. To gain more detail in the primary region of operation, a higher-resolution scan was performed for high and low times between 0 μ s and 400 μ s.

The characterization revealed a non-trivial relationship between the PWM parameters and the output voltage. A pre-calibrated lookup table could be used to account for the non-trivial relationship between the PWM parameters and the output voltage. However, acquiring a sufficiently detailed map for all possible operating conditions would be too time-consuming. But more importantly, as established in the previous section, the output voltage is also dependent on the illumination power. This means that any static lookup table would be valid only for a single, specific illumination condition, rendering this approach infeasible for the experiment. These limitations motivated the implementation of the PID control loop discussed in Section 3.5.

3.5. PID Control Loop

The characterization in the previous section revealed that an open-loop control approach using a static lookup table would be impractical due to the output voltage's strong dependence on illumination power. To achieve precise and reproducible voltage settings regardless of external conditions, a closed-loop PID control system was implemented in the control software.

The control strategy is to modulate the PWM high-time to adjust the output voltage, while the low-time is held constant. As seen in the voltage map (Figure 3.5), this creates a more predictable relationship where increasing the high-time always decreases the output voltage. However, a single fixed low-time cannot provide good resolution and stability across the entire desired voltage range.

To address this, the control algorithm uses two distinct operating regimes, each optimized for a different voltage range. The software automatically selects the appropriate regime based on the target voltage:

- High-Voltage Range (0.6 V to 7.8 V): For this range, a fixed low-time of 75 μ s is used. This covers a wide control range with a sufficiently high voltage resolution per tick.
- Low-Voltage Range (< 0.6 V): To achieve finer control and a stable 0 V output, which is not possible in the high-voltage regime, a longer low-time of 375 μ s is used. This shifts the characteristics of the charge pump to enable a higher resolution at very low output voltages.

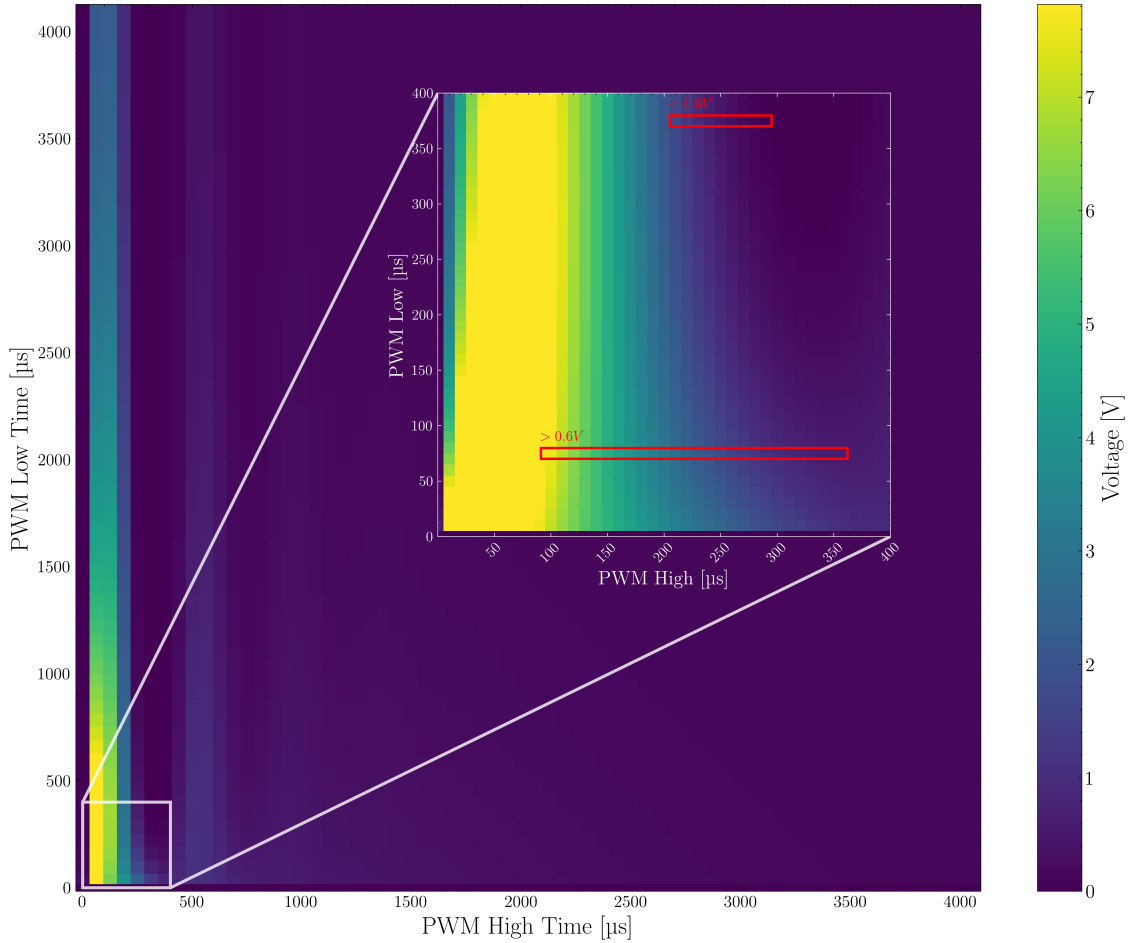


Figure 3.5.: Mapping of the charge pump output voltage as a function of PWM high-time and low-time. The non-linear relationship necessitates a closed-loop control system. The red-highlighted regions indicate the two operating regimes used by the PID control system as described in the next section, optimized for high-voltage and low-voltage control, respectively.

These distinct characteristics are visualized in Figure 3.6. Each regime uses its own set of pre-tuned PID parameters (K_p , K_i , K_d) to ensure optimal performance.

When a new target voltage is requested, the control algorithm makes an initial estimate of the required high-time to rapidly approach the setpoint, after which the PID controller performs the fine-tuning. The system is considered stable once the measured voltage remains within a tolerance of ± 5 mV of the target for a duration of 5 seconds. This robust stability check ensures that measurements are only performed once the voltage has truly settled. The entire process of reaching and stabilizing a new voltage setpoint typically takes around 10 seconds.

The final accuracy of 5 mV is not limited by the ADC's theoretical resolution, but rather by the discrete voltage step associated with a single-tick change in the PWM high-time within the selected operating regime. While this could be improved by selecting longer regimes, the current accuracy is more than sufficient for the requirements of the retarding grid measurements performed in this thesis.

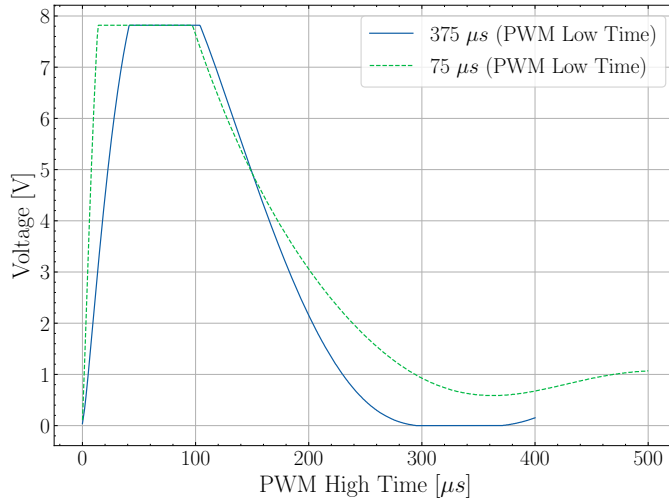


Figure 3.6.: Output voltage of the charge pump as a function of PWM high-time for the two distinct operating regimes used by the PID controller. The regime with a 75 μ s low-time (orange) offers a wide control range and a less steep voltage decline, making it suitable for the high-voltage range (0.6 V to 7.8 V). In contrast, the regime with a 375 μ s low-time (blue) enables fine control down to 0 V but exhibits a steeper voltage change at higher high-times, making it ideal for the low-voltage range (< 0.6 V). The observed voltage cutoff at 7.81 V is due to the maximum measurable voltage of the onboard ADC.

4. Beam Optimization

All optimization procedures described in this chapter were performed using the W(111) single-crystal sample.

4.1. Magnetic Coil optimization

The installation of the electrostatic lens system required a complete disassembly and reassembly of the sample chamber of the SLOPE beam apparatus. This intervention and the introduction of new electrodes within the chamber altered the optics for the positron beam. Therefore, a re-optimization of the currents in the magnetic correction coils was necessary to ensure proper alignment of the incident beam. The established beam alignment technique, detailed in the work of Suhr [16], was incompatible with the new experimental configuration, since it uses a special positioning sampleholder.

Therefore, an alternative optimization strategy was employed. The procedure involved a two-dimensional scan of the currents supplied to the final vertical (C4V) and horizontal (C4H) magnetic correction coils. During this scan, coincidence count rates were recorded simultaneously from two detector systems: the HPGe detectors positioned at the sample and the scintillation detectors at the dump lens. This entire two-dimensional scan was performed under two distinct conditions: first with a retarding grid potential of 0 V, and then repeated with a potential of 7 V. The purpose of this two-condition measurement was to distinguish the signal of the primary incident positron beam from that of the low-energy positrons reemitted from the sample surface. At a retarding potential of 0 V, both the primary beam (if it misses the sample) and any reemitted positrons are able to reach the dump lens. Conversely, applying a 7 V potential is sufficient to repel the low-energy reemitted positrons, preventing them from reaching the dump lens. In this configuration, only the primary beam can generate a signal at the dump. By comparing the signals from both detector systems under these two voltage conditions, the optimal coil settings for aligning the beam onto the sample can be determined.

The results of these scans are presented in Figure 4.1. Event counts from the HPGe detectors, shown in Figures 4.1a and 4.1b, show a distinct maximum in the coincidence rate at approximately 1.7 A for C4H and 2.4 A for C4V. This peak corresponds to the coil settings that optimally position the incident positron beam onto the sample surface, maximizing the annihilation events at that location. A slight reduction in the maximum count rate is observable at the 7 V setting compared to the 0 V setting, which can be

4. Beam Optimization

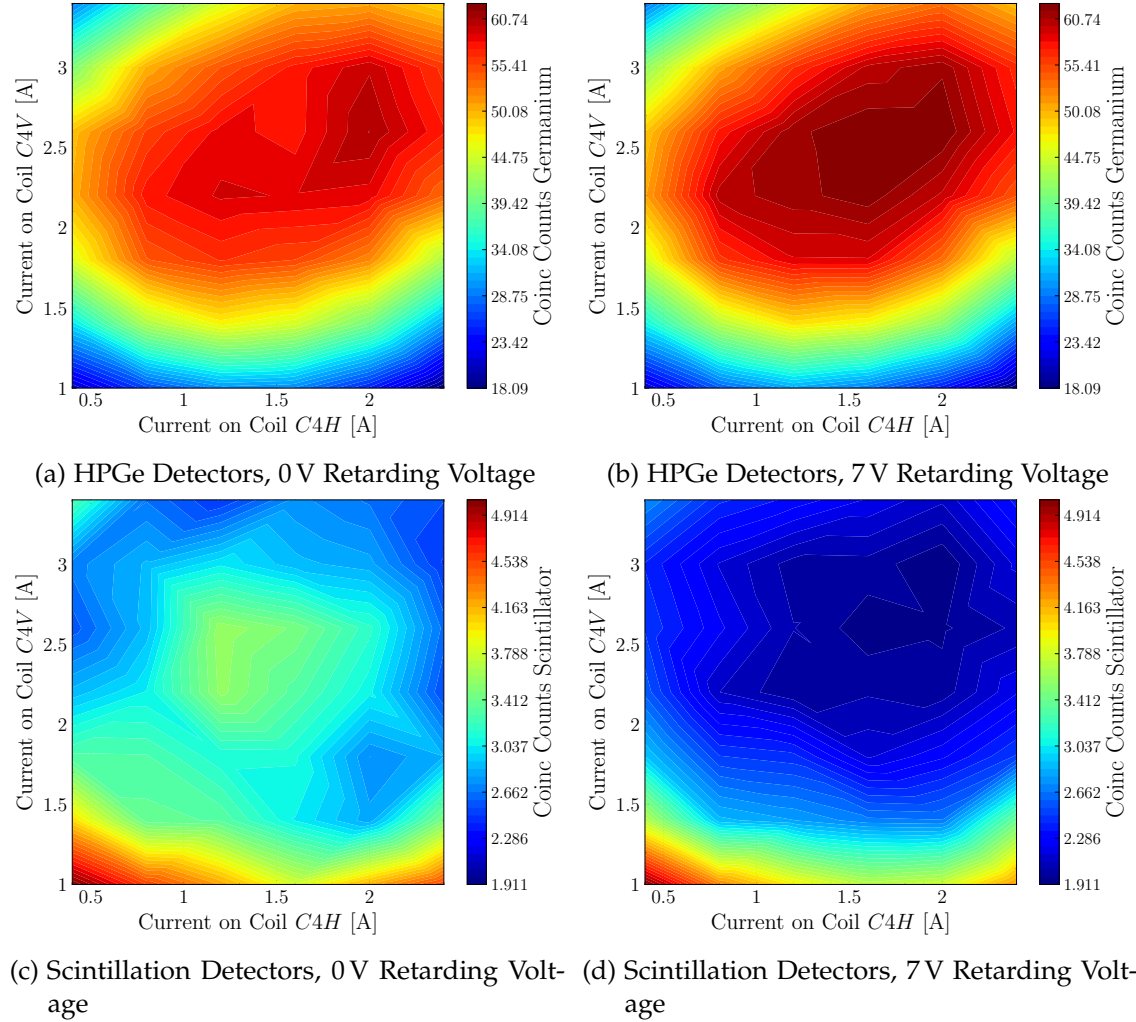


Figure 4.1.: Two-dimensional maps of coincidence count rates as a function of the C4H and C4V correction coil currents at 3 keV. The top row (a, b) shows data from the HPGe detectors, indicating annihilations on the sample. The bottom row (c, d) shows data from the scintillation detectors, indicating annihilations on the dump lens. Measurements were performed with retarding grid potentials of 0 V (left column) and 7 V (right column) to distinguish between incident and reemitted positrons.

4.1. Magnetic Coil optimization

attributed to the reimplantation of reemitted positrons. However, this effect was not investigated further during this optimization step.

Event counts from the scintillation detectors are shown in Figures 4.1c and 4.1d. In both maps, high count rates are visible at the border of the scan area. These regions correspond to coil settings where the primary beam misses the sample and strikes the dump lens assembly instead. A localized region of elevated count rate is present near the center of the map (approximately 1.4 A for C4H and 2.2 A for C4V) only when the retarding potential is 0 V. This signal vanishes completely when the retarding potential is increased to 7 V. This behavior confirms that the central spot originates from low-energy remoderated positrons emitted by the sample, which pass through the 0 V grid and are guided onto the dump lens.

To isolate and locate the signal from the reemitted positrons, a difference map was generated by subtracting the 7 V count rate data from the 0 V data. The result, shown on the left in Figure 4.2, clearly highlights the optimal coil configuration for guiding the incoming beam onto the sample. Based on these findings, an additional, higher-resolution scan was performed in the vicinity of this peak, which determined the optimal coil currents to be 1.6 A for the C4H coil and 2.6 A for the C4V coil, as seen in Figure 4.2 on the right.

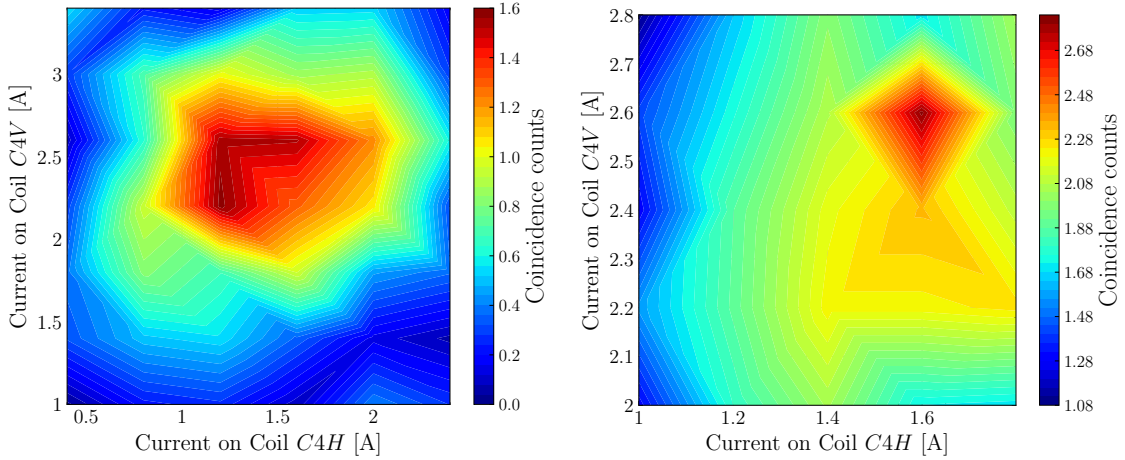


Figure 4.2.: Difference maps of the scintillation detector coincidence count rates (0V data minus 7V data). Both plots isolate the signal from reemitted positrons, showing a maximum that indicates the optimal coil settings for the setup. On the left is the low-resolution scan, and on the right is the high-resolution scan.

4.2. Lens Voltage Optimization

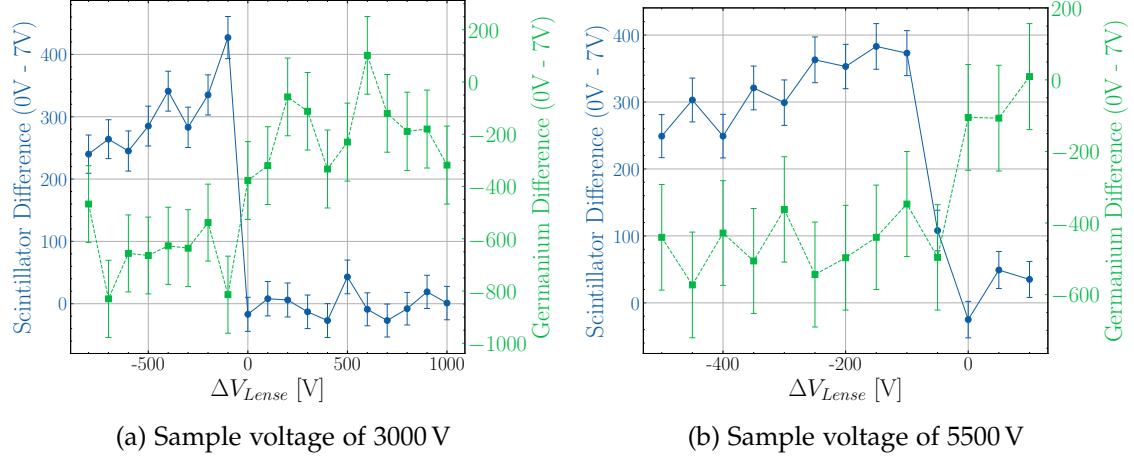


Figure 4.3.: Coincidence count rates of the Scintillator (Blue) and the Germanium (Green) Detector Pair as a function of the voltage ΔV_{Lens} between sample and dump lens for 3 keV (left) and 5.5 keV (right) implantation energy. A clear peak in the scintillator signal is observed at $\Delta V_{\text{lens}} \approx -100$ V in both scans, confirming the optimal setting is independent of the sample voltage. Each data point represents a 3-minute long measurement.

The dump lens (L2) voltage must generate an attractive potential that guides positrons past the retarding grid to the annihilation spot in front of the scintillation detectors. A scan was performed to determine the optimal voltage.

During this scan, the dump lens voltage relative to the sample potential (ΔV_{lens}) was varied. To isolate the signal coming from remoderated positrons, measurements were conducted at two retarding grid potentials: 0 V (allowing remoderated positrons to pass) and 7 V (repelling them). The difference in the coincidence count rates between these two settings provides a measure of the remoderated positron flux reaching the dump. The results of this scan (using an acceleration voltage of 3000 V) are presented in Figure 4.3(a).

As expected, a positive potential on the dump lens relative to the sample results in a negligible signal, as positrons are repelled before reaching the lens. For negative potentials, a clear signal emerges, peaking at a relative voltage of approximately -100 V. Correspondingly, the signal from the HPGe detectors shows a similar decrease in this region. This is consistent with fewer remoderated positrons being re-implanted onto the sample and instead being successfully guided to the dump.

To test whether this optimum is independent of the primary beam energy, the scan was repeated at a sample voltage of 5500 V, as shown in Figure 4.3(b). The results show a

similar trend, indicating that the optimal relative dump lens voltage is not significantly dependent on the sample potential.

Based on these measurements, the optimal dump lens potential is -100 V relative to the sample. However, during initial experiments, a concern was raised that using lower voltage differences could increase susceptibility to electronic noise. While this concern couldn't be confirmed, as a precaution the initial spectrum measurements were performed at a more conservative setting of -400 V. To ensure consistency across all datasets presented in this work, this potential of -400 V was maintained for all subsequent measurements. As shown in Figure 4.3, the remoderated positron signal at -400 V is only slightly reduced compared to the optimum, validating this choice as an acceptable compromise that does not significantly impact the quality of the measurements.

5. Investigation of the Energy Spectrum and Yield of Positrons after Remoderation

In this chapter, the measurements of the low-energy positron reemission spectrum for three different moderator materials are presented: tungsten (W(111)), annealed polycrystalline nickel (Ni), and annealed polycrystalline platinum (Pt). For each material, two types of measurements were done: the energy spectrum of the remoderated positrons and the reemission yield as a function of the primary beam's implantation energy.

5.1. Measurement Procedures

5.1.1. Reemission Spectrum Measurement

To determine the kinetic energy distribution of the remoderated positrons, the primary positron beam was accelerated to a fixed implantation energy by applying a constant negative bias to the sample holder while the retarding grid potential was varied. The retarding grid voltage was varied in discrete steps. At each voltage step, the potential was set and stabilized using the PID control loop of the active sampleholder. Following stabilization, the coincidence count rate of annihilation events was recorded for a fixed duration by the BGO scintillation detectors aimed at the beam dump. This procedure generates an integral energy spectrum, as only those positrons with a kinetic energy component normal to the surface greater than the applied retarding potential can overcome the barrier and reach the dump to be detected. To detect possible systematic errors, the voltage steps were not performed sequentially but in a bit-reversed order, ensuring that points that are adjacent in time are distant in voltage. The differential energy spectrum, which represents the kinetic energy distribution of the remoderated positrons, can then be obtained by calculating the negative derivative of the measured integral curve with respect to the retarding voltage.

5.1.2. Reemission Yield Measurement

To measure the Reemission Yield, the countrate of the scintillation detectors as a function of the implantation energy was recorded. To isolate the signal from remoderated positrons against the background signal at the dump detectors, two measurements were performed for each implantation energy: In the first, a positive, repelling potential of +7 V was applied to the retarding grid by the active sampleholder. This potential should prevent any low-energy remoderated positrons from passing through to the dump

lens. The coincidence count rate measured by the BGO detectors in this configuration, therefore, corresponds to the background level. In the second, the retarding grid potential was set to 0 V relative to the sample. Now, remoderated positrons are able to pass through the grid and are guided to the dump. The count rate recorded during this step represents the sum of the remoderated positron signal and the background. The net signal is then calculated by subtracting the background count rate (measured at +7 V) from the total count rate (measured at 0 V).

5.2. Tungsten

The measurements for tungsten were performed on a single-crystal W(111) sample. The crystal was grown by electron-beam zone melting at the Institute of Solid State Physics in Chernogolovka, Russia, and cut into a 10x10x1 mm³ sample. It was subsequently prepared through mechanical and chemo-mechanical vibration polishing. Prior to installation in the experimental chamber, the sample was cleaned in an ultrasonic bath with high-purity acetone and annealed at 2000 K for 3 minutes.

5.2.1. Reemission Spectrum

The reemitted positron spectrum of a single-crystal W(111) sample was measured across the full retarding potential range from 0 to 7 V. Using a positron implantation energy of 3000 eV and a measurement time of three minutes per voltage step, this coarse scan is shown in Figure 5.1. It shows a signal from remoderated positrons which becomes indistinguishable from the background at retarding potentials above approximately 3 V.

Consequently, three high-resolution measurements were performed in the 0–3 V range, with the integration time increased to 10 minutes per step. The results are shown in Figure 5.2(a). The count rates show consistent behavior across scans, indicating that no obvious systematic errors were present during the measurements. The data from the HPGe detectors show a corresponding increase in count rate as the scintillator signal decreases. This inverse relationship is attributed to retarded positrons being re-implanted into the sample, although this signal is not used for the primary analysis due to its lower signal-to-noise ratio.

The three datasets were added together, resulting in an integral spectrum with three times more statistics. The differential energy spectrum, $\frac{dN}{dE}$, is proportional to the negative derivative of this integral spectrum. To minimize noise that would be amplified during differentiation, the combined data was first smoothed using a five-point moving average filter to minimize noise that would be amplified by numerical differentiation. Figure 5.2(b) shows the final combined integral spectrum, its smoothed curve, and the derived differential energy spectrum.

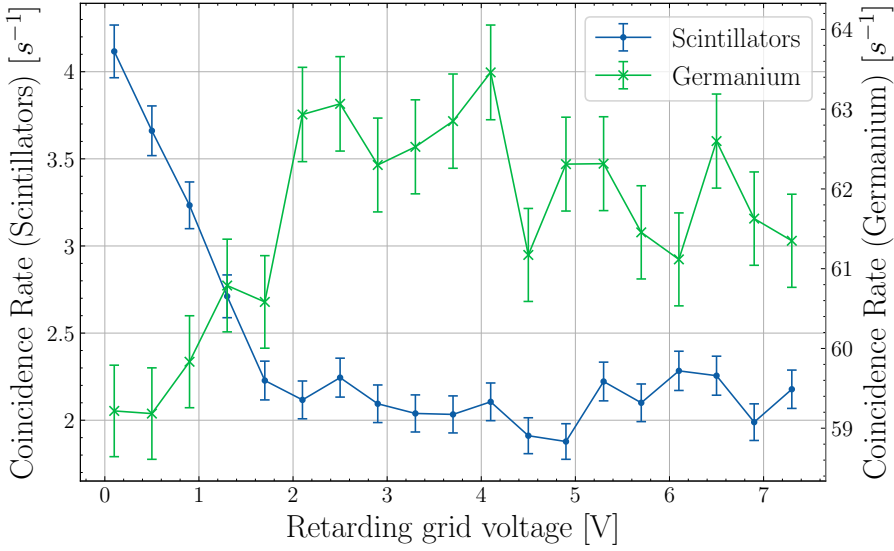


Figure 5.1.: Integral energy spectrum of W(111) measured across the full voltage range of the active sample holder. The coincidence count rate at the scintillators (SLA x SLB) and the HPGe (OAH x OAB) is shown as a function of the retarding grid potential. Above approximately 3 V, the signal reaches a constant background level, marking the relevant energy window for further measurements.

The maximum kinetic energy of the remoderated positrons was determined using a statistical indicator on the Poisson distribution. The signal in the region $V > 2.2$ V was assumed to consist only of background events. The mean count rate in this region was used to establish the expected mean count (μ) of a background-only process. The probability of observing k counts in a measurement, assuming it originates from this background process, is given by the Poisson Probability Mass Function (PMF):

$$P(k; \mu) = \frac{e^{-\mu} \mu^k}{k!}$$

where k is the measured integer count for a given voltage step and μ is the expected mean background count for the measurement duration. A low probability suggests the measured count is statistically unlikely to be a background fluctuation, thus indicating the likely presence of a true signal. [21]

This probability was calculated for each point in the spectrum, as plotted in Figure 5.3. The curve shows a sharp probability drop as the true positron signal emerges from the background noise. Using a significance threshold of 10^{-4} , the cutoff energy is determined to be $1.87(10)$ V.

5. Investigation of the Energy Spectrum and Yield of Positrons after Remoderation

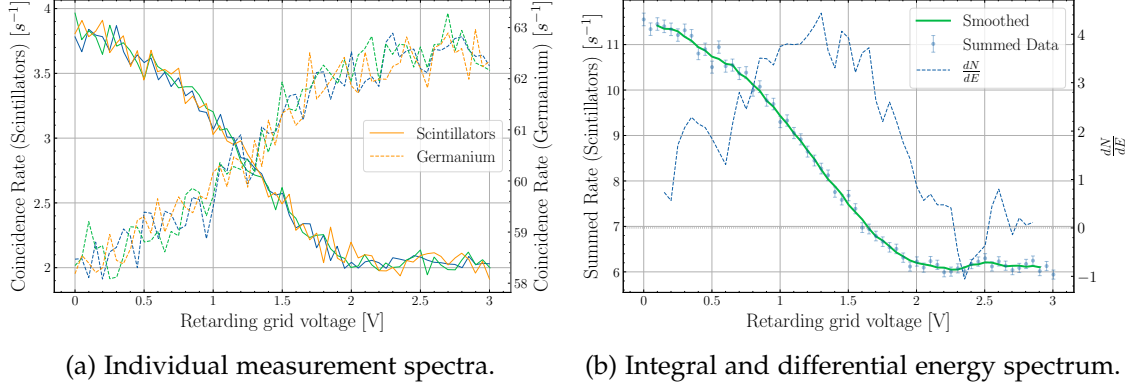


Figure 5.2.: Integral and differential energy spectra of remoderated positrons from W(111). (a) Three independent measurements showing no systematic error. The primary y-axis (left) shows the signal from the scintillation detectors (SLA x SLB), while the secondary y-axis (right) shows the signal from the HPGe detectors (OAH x OAB). (b) The combined and smoothed integral spectrum (green line) with the raw summed data points (blue markers). The corresponding differential energy spectrum (dN/dE) is shown as a dashed blue line.

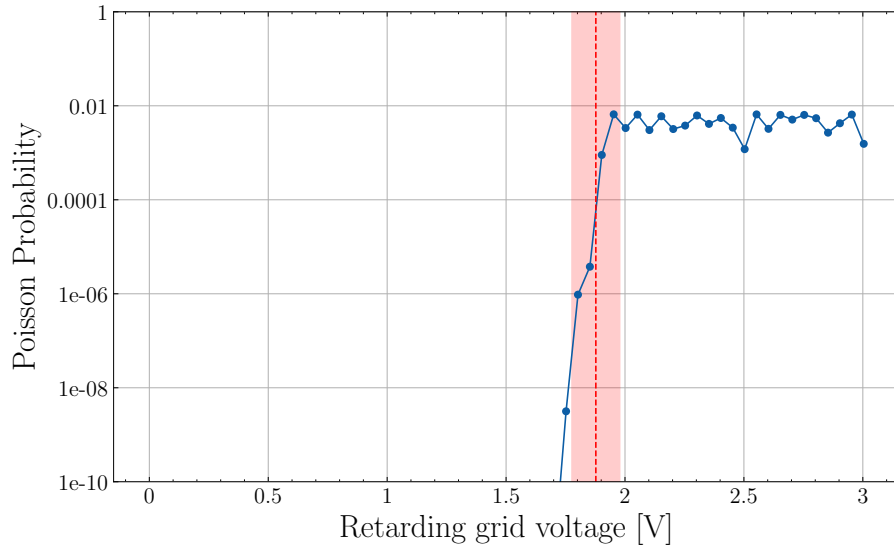


Figure 5.3.: Determination of the cutoff energy for W(111) using Poisson statistics. The plot shows the probability of the background process producing the observed count at each retarding grid potential. The sharp drop indicates the start of the true positron signal. The cutoff energy is determined to be 1.87 ± 0.1 V, marked by the red dashed line and confidence interval.

5.2.2. Reemission Yield

Reemission yield measurements were performed by scanning the implantation energy from 400 eV to 5600 eV, with a measurement time of 10 minutes per point. The results for both the HPGe and the scintillation detectors are presented in Figures 5.4(a) and 5.4(b), respectively. Both sets of raw data show no obvious systematic errors and indicate the annihilation of low-energy positrons on the dump electrode due to the separation between the 0 V and 7 V retarding grid measurements.

In the HPGe detector data (Figure 5.4(a)), a general downward trend in count rate is observed for lower implantation energies, with a slight increase between 400 eV and 800 eV. This trend is consistent for both retarding grid voltages, suggesting it is primarily influenced by the incident beam characteristics rather than a change in the reemitted positrons.

The scintillation detectors (Figure 5.4(b)) recorded an upward trend in count rate, which is visible for lower implantation energies when the retarding grid voltage is held at 0 V. The background signal, with the retarding grid voltage held at 7 V, shows a noticeable but less significant increase in count rate at low implantation energies.

To isolate the reemission signal from the background, measurements with a retarding potential of 7 V were subtracted from those at 0 V, and the absolute differences are plotted in Figures 5.4(c) and 5.4(d). Both plots show a general increase in the reemitted positron yield as the implantation energy decreases, which is consistent with the theoretical expectation that positrons implanted closer to the surface have a higher probability of diffusing back. However, the trend is not monotonic. A slight increase is observed down to approximately 1.5 keV, below which the yield increases much more steeply. Furthermore, the scintillator data (Figure 5.4(d)) exhibits a local minimum around 800 eV. This dip is likely due to a change in the beam's characteristics at low energies. The combination of decreasing scintillator counts (fewer positrons reaching the dump) only at 0V, but not at 7V and the corresponding increase in raw HPGe counts at the sample (Figure 5.4(a)) suggests that a smaller fraction of the incident beam is hitting the sample to be remoderated, thus reducing the net reemission signal in this specific energy range.

While the standard model for thermal positron reemission can explain the general trend, it fails to account for the steepness of the observed rise below 1.5 keV. To account for this discrepancy, a model including the contribution from epithermal positrons was employed, as introduced in Section 1.3.4. Figure 5.5 compares the measured net reemission yield with the theoretical back diffusion probability. The total reemission yield is modeled as the sum of two components: the fraction of thermalized positrons that diffuse back to the surface, and the fraction of epithermal positrons that scatter back before thermalization.

As the figure demonstrates, the combined theoretical curve provides a much better fit to the experimental data. The model uses a thermal diffusion length of $L_+ \approx 138 \text{ nm}$, taken from Dryzek et al. [8], and an epithermal scattering length of $l_+ \approx 2 \text{ nm}$. This value for the scattering length was taken from Britton et al. for molybdenum and is used here as a reasonable estimate [11]. This result suggests that the enhanced signal at low implantation energies is not solely an instrumental artifact, but has a physical basis in the emission of epithermal positrons. The short scattering length means that only positrons stopped within the first few nanometers of the surface contribute significantly to this epithermal signal, explaining its dominance at very low implantation energies.

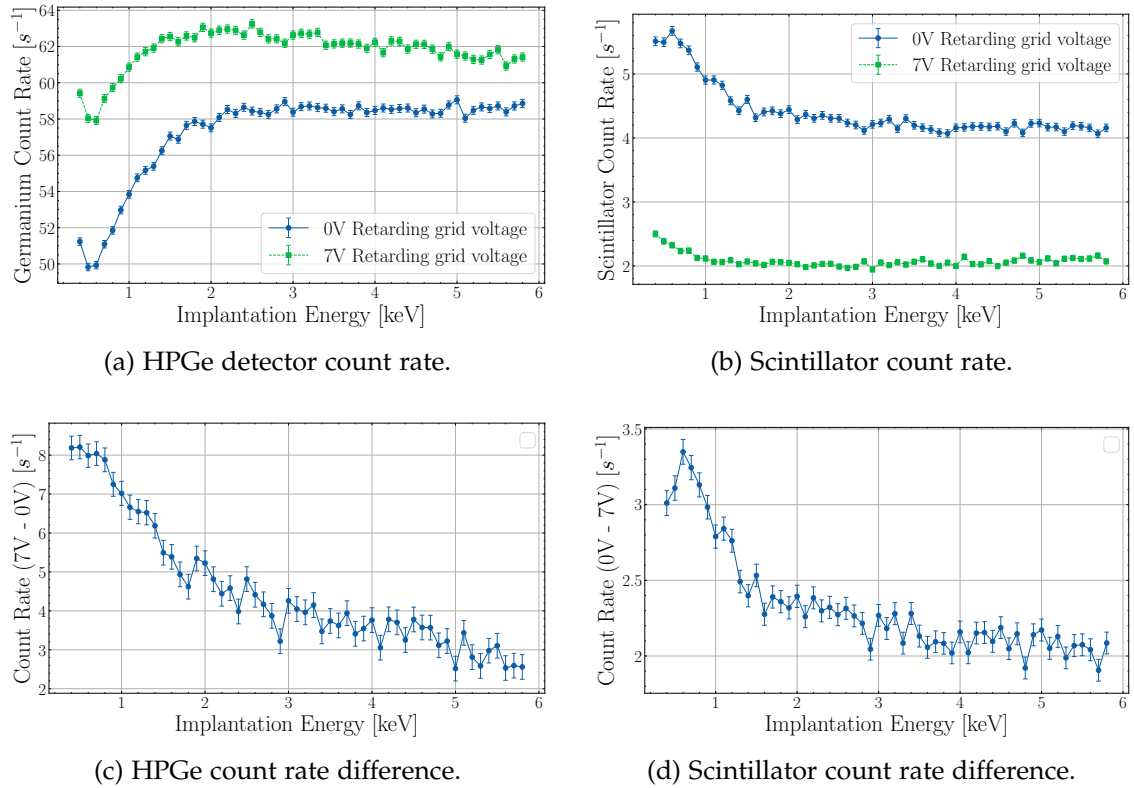


Figure 5.4.: Positron reemission yield for W(111) as a function of implantation energy. (a) and (b) show the raw coincidence count rates for the HPGe and scintillation detectors, respectively, at 0 V and 7 V retarding grid potentials. (c) and (d) display the difference in count rates for the HPGe and scintillation detectors, isolating the signal from reemitted positrons.

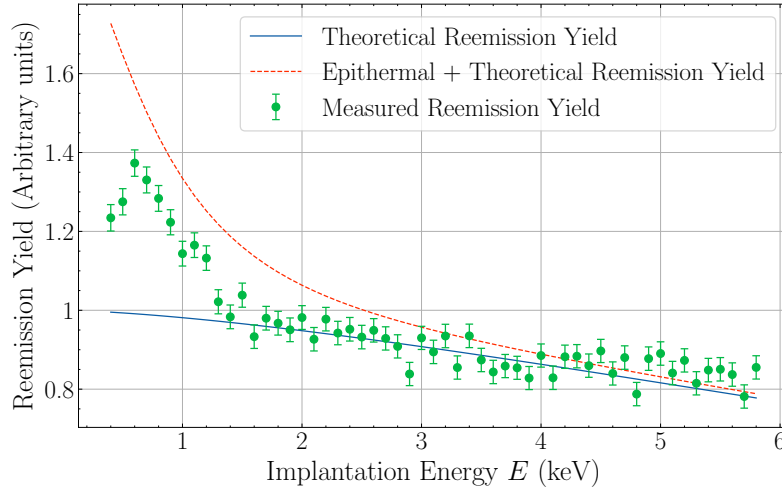


Figure 5.5.: Comparison of the measured reemission yield for W(111) with theoretical models. The solid blue line represents the calculated backscattering yield considering only thermalized positrons, which fails to match the data at low energies. The dashed red line includes an additional contribution from epithermal positrons, modeled according to Britton 1988 [11]. The combined model shows significantly better agreement with the measured data (orange points), particularly below 2 keV.

5.3. Nickel

The sample used for the nickel measurements was a high-purity (99.98%) polycrystalline nickel, which was prepared and characterized in the bachelor's thesis of Porth [22]. The final preparation of the sample involved mechanical polishing followed by vacuum annealing at 975 °C to reduce the concentration of defects and ensure a clean metallic surface. During the sample change to Nickel, the alignment magnetic coils were moved, necessitating a re-optimization of the magnetic coil currents as described in Section 4.1. The new optimal settings were determined to be 1.3 A for C4H and 2.2 A for C4V. Unfortunately, a magnetic guiding coil failed during the measurement and the malfunction was only discovered later during the platinum measurements. This issue significantly limited the amount of reliable data that was acquired for Nickel.

5.3.1. Reemission Spectrum

The reemission spectrum for Nickel was measured with an implantation energy of 1000 eV and a measurement time of 20 minutes per point across a retarding grid voltage range of 0-3 V. This measurement was performed before the magnetic coil failure. As shown in Figure 5.6, a slight increase in count rate for lower retarding grid voltages can be observed in the scintillation detectors. However, due to the limited data, a comprehensive data analysis, including the differentiation of an integral spectrum, was not possible.

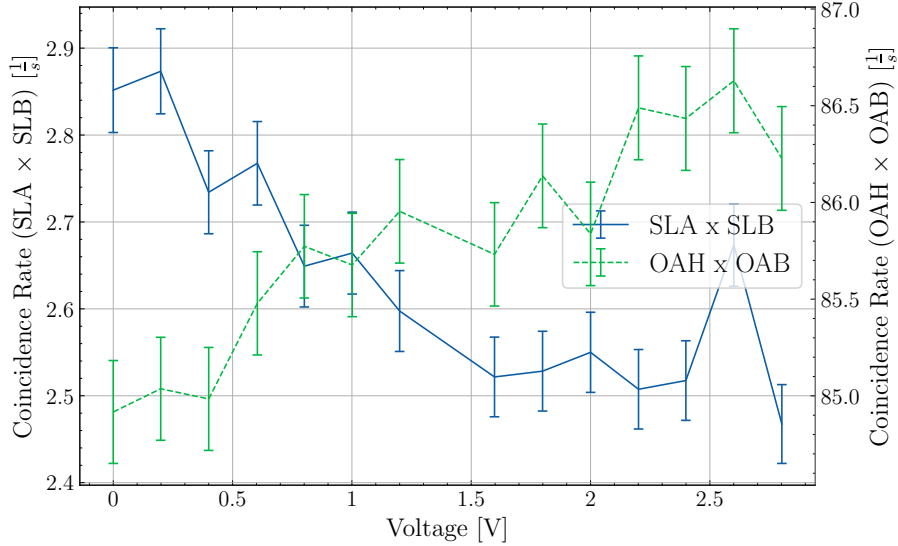


Figure 5.6.: Integral energy spectrum of remoderated positrons from Nickel (Ni) at 1000 eV implantation energy. The coincidence count rate at the scintillators (SLA x SLB) and the HPGe (OAH x OAB) is shown as a function of the retarding grid potential. A slight increase in scintillator count rate is visible at lower voltages.

5.3.2. Reemission Yield

Only one valid reemission yield measurement series was obtained for Nickel. The data is presented in Figures 5.7(a) and 5.7(b) for the HPGe and scintillation detectors, respectively. Both detectors show a general increase in count rate for lower implantation energies. In the HPGe data, a slight decrease in count rate around 400 eV is observed, similar to the behavior seen in the tungsten measurements.

In the HPGe data, a slight decrease in count rate around 400 eV is observed, again mirroring the behavior seen in the tungsten measurements. This is likely the same instrumental artifact related to beam transport optics at very low energies, rather than a physical property of nickel. Figures 5.7(c) and 5.7(d) display the difference in count rates between 0 V and 7 V retarding grid voltages, isolating the reemitted positron signal. This increase can probably be attributed to the reemission of epithermal positrons.

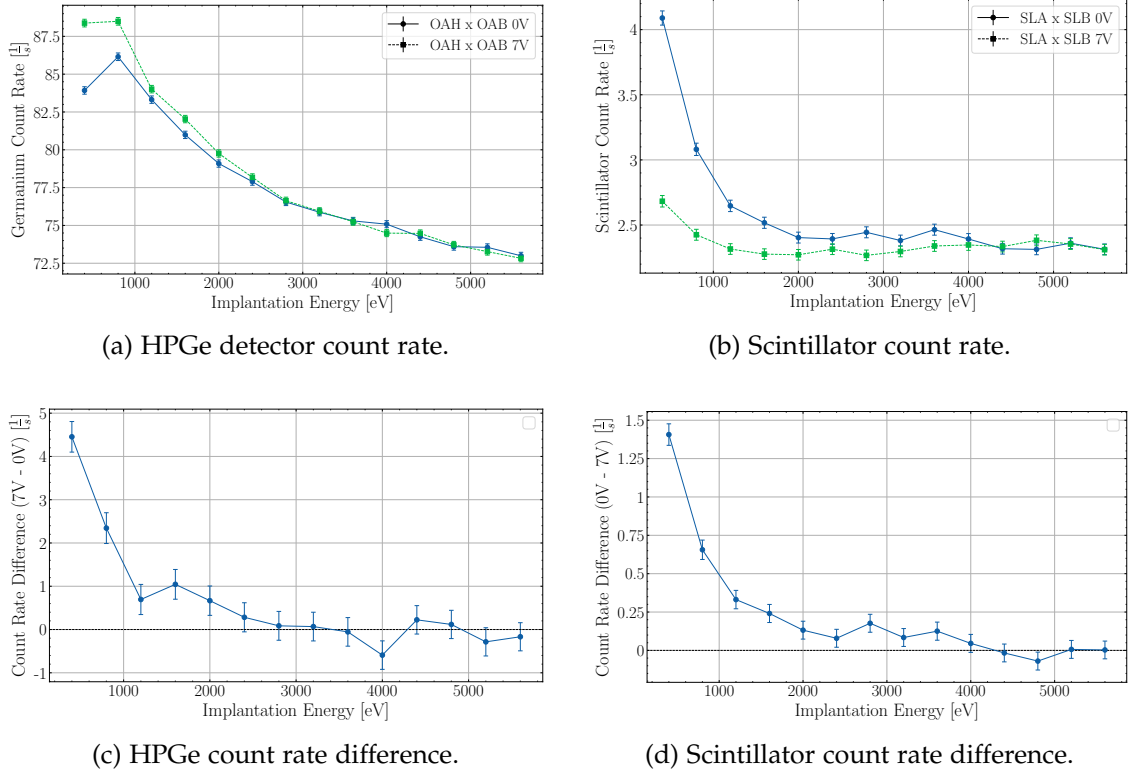


Figure 5.7.: Reemission yield for Nickel (Ni) as a function of implantation energy. (a) and (b) show the raw coincidence count rates for the HPGe and scintillation detectors, respectively, at 0 V and 7 V retarding grid potentials. (c) and (d) display the difference in count rates for the HPGe and scintillation detectors, isolating the signal from reemitted positrons.

5.4. Platinum

For the platinum investigation, an annealed polycrystalline platinum sample was used. Further details regarding its purity, grain size, and the specific annealing procedure were not available. Similar to the Nickel measurements, a re-optimization of the magnetic coils was performed for Platinum, yielding the same optimal parameters: 1.3 A for C4H and 2.2 A for C4V. The faulty magnetic guiding coil was discovered towards the end of the platinum measurement series, which also limited the amount of reliable data collected for this material.

5.4.1. Reemission Spectrum

Only one reemission spectrum measurement for Platinum wasn't affected by the malfunction, conducted with a 3000 eV implantation energy and a measurement time of 20 minutes per point. This measurement was unfortunately interrupted mid-series due to a server failure, resulting in a pause of several hours. The data acquired before the interruption is plotted in blue, and the data after the interruption is in green in Figure 5.8. The shift between the two parts suggests that a systematic error occurred during the server failure, rendering this data unsuitable for a quantitative analysis of the reemission spectrum. Nevertheless, a small increase in count rate near 0 V retarding grid potential can still be observed, indicating that further, uninterrupted measurements could potentially reveal a meaningful reemission spectrum in this area.

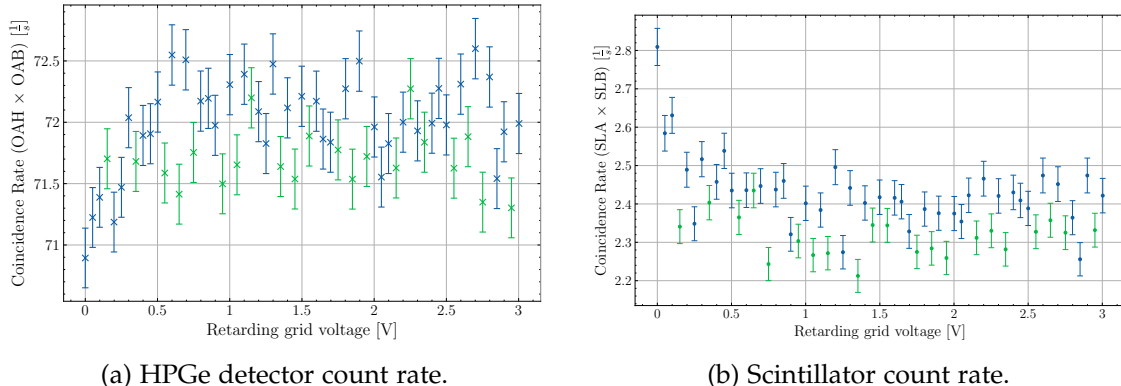


Figure 5.8.: Integral energy spectrum of remoderated positrons from Platinum (Pt) at 3000 eV implantation energy. The blue and green points represent data collected before and after a server interruption, respectively. A systematic shift is visible, making the data unsuitable for detailed analysis.

Reemission Yield

For the reemission yield of Platinum, also only one measurement wasn't affected by the malfunction, with a measurement time of 15 minutes per point. The data is presented in Figures 5.9(a) and 5.9(b). Similar to previous materials, an increase in the general count rate is observed for lower implantation energies in both detectors. The HPGe detector (Figure 5.9(a)) shows a drop in count rate near 1000 eV and a slight increase again at 400 eV, a trend consistent with the tungsten measurements and likely related to beam optics.

When examining the difference spectrum (Figures 5.9(c) and 5.9(d)), no clear signal from reemitted positrons for implantation energies is present in the data above 2000 eV. At lower energies, however, a steep increase in the count rate is observed below 2000 eV. While the data is noisy due to the limited measurement time, this sharp rise is consistent with the behavior observed for tungsten and nickel. It is therefore plausible that this signal represents the contribution from epithermal positrons, which becomes the dominant reemission channel at very low implantation energies. Although the data quality precludes a quantitative fit, the qualitative trend strongly supports the epithermal emission model.

5.5. Background

To investigate some of the unexplained trends observed in the reemission yield measurements, a background measurement was conducted with no sample installed in the chamber; instead, the positron beam was directed onto the copper plate, on which the samples are normally mounted. The primary goal was to identify any influences of the experimental setup on the behavior of positrons or background noise. It is important to note that these background measurements could not be directly subtracted from the sample measurements to obtain background-reduced results, as the overall count rates slightly changed after each sample change and subsequent re-alignment of the beam.

5.5.1. Reemission Spectrum

The background reemission spectrum was measured from 0-3 V with a measurement time of 20 minutes per point and an implantation energy of 3 keV. As depicted in Figure 5.10, the count rate for both the HPGe and scintillation detectors remained constant and independent of the retarding grid voltage. This observation confirms that the retarding grid itself does not introduce any voltage-dependent background noise.

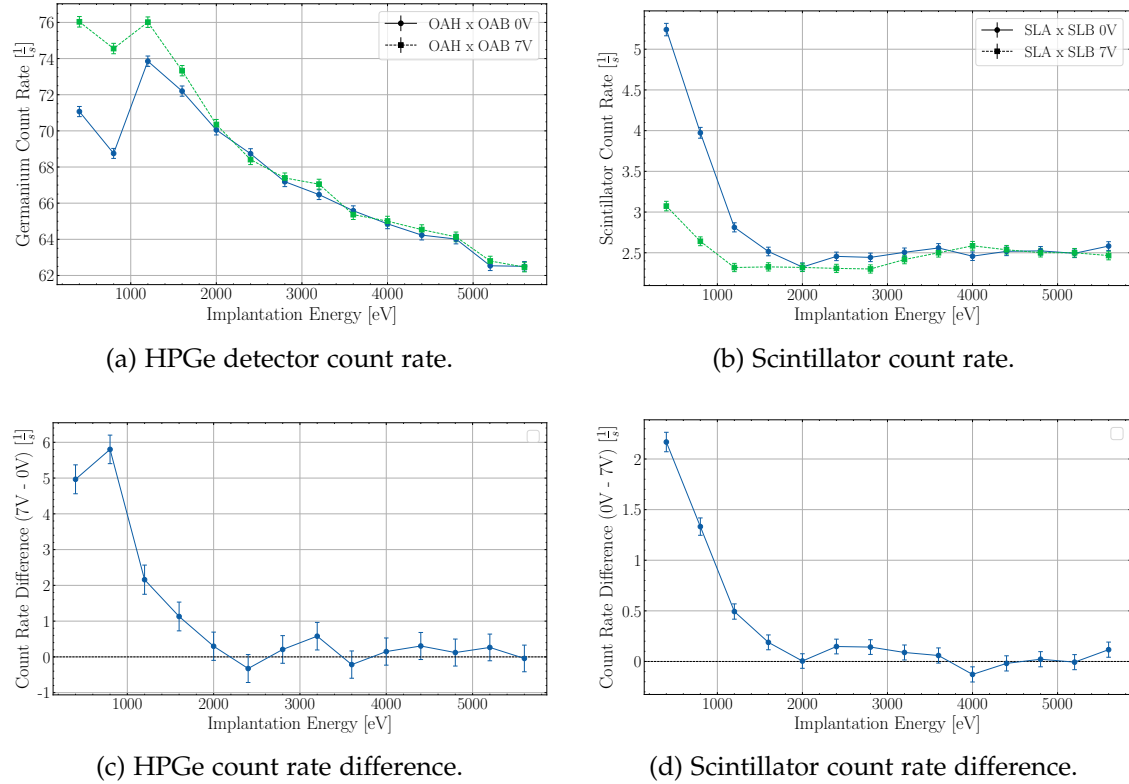


Figure 5.9.: Reemission yield for Platinum (Pt) as a function of implantation energy. (a) and (b) show the raw coincidence count rates for the HPGe and scintillation detectors, respectively, at 0 V and 7 V retarding grid potentials. (c) and (d) display the difference in count rates for the HPGe and scintillation detectors, isolating the signal from reemitted positrons.

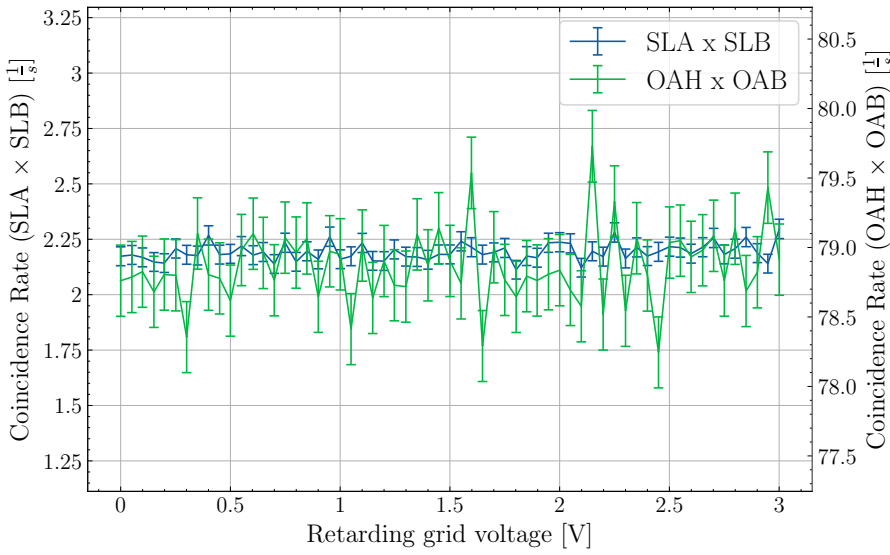


Figure 5.10.: Background spectrum measured with no sample installed. The coincidence count rate at the scintillators (SLA x SLB) and the HPGe (OAH x OAB) is shown as a function of the retarding grid potential. The count rates are constant, indicating no influence of the retarding grid on background noise.

5.5.2. Reemission Yield

The background reemission yield measurements are presented in Figures 5.11(a) and 5.11(b). For the HPGe detectors (Figure 5.11(a)), a general decrease in count rate is observed, largely independent of the retarding grid voltage. However, below 1000 eV implantation energy, a lower count rate is observed at 0 V retarding grid voltage compared to 7 V.

This observation was initially interpreted as the retarding grid influencing background noise. However, a more physical explanation is that this ‘background’ measurement is, in fact, detecting a weak reemission signal from the copper mounting plate itself. Copper is known to have a negative positron work function and can act as a positron moderator. The difference signal, highlighted in Figure 5.11(c), is most pronounced below 1000 eV, which is consistent with the energy range where epithermal emission from the copper surface would be most significant. This suggests that even in the absence of a dedicated sample, a baseline level of positron reemission occurs from the sample holder, dominated by the epithermal component at low energies. The scintillation detector data (Figure 5.11(b) and (d)) show no effect, which could be due to the lower reemission efficiency of the un-annealed copper surface compared to the prepared samples.

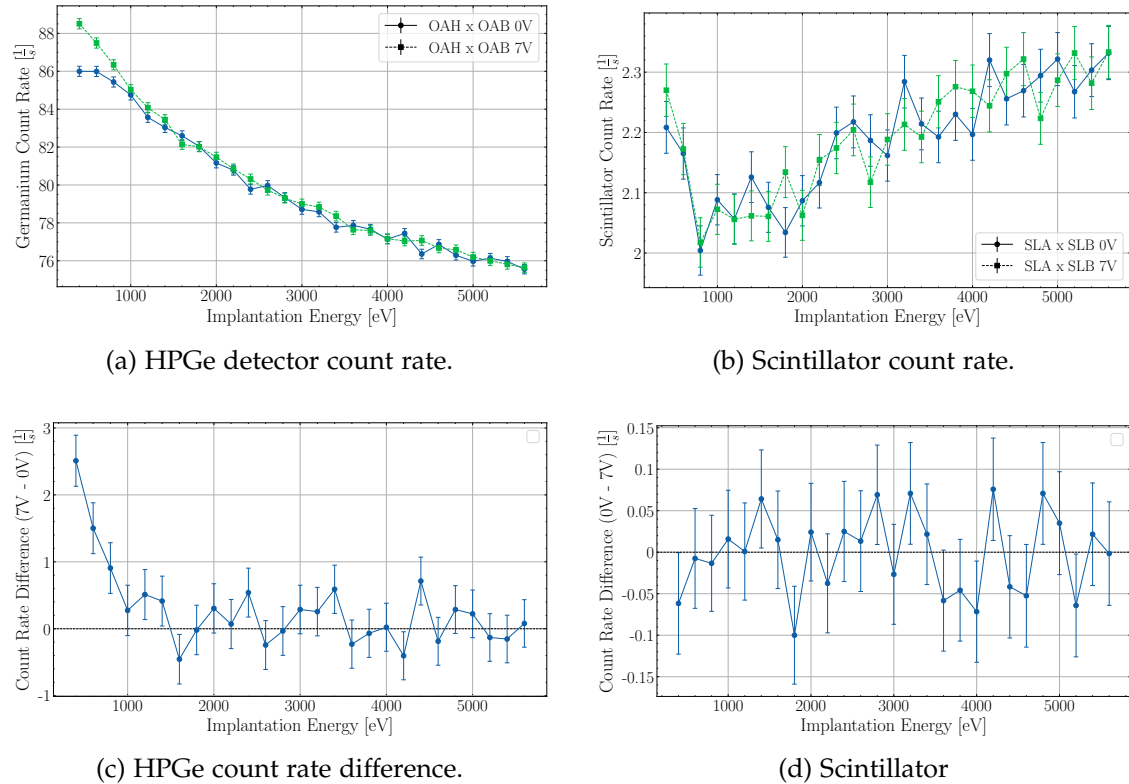


Figure 5.11.: Background yield measured with no sample installed. (a) and (b) show the raw coincidence count rates for the HPGe and scintillation detectors, respectively, at 0V and 7V retarding grid potentials. (c) and (d) display the difference in count rates for the HPGe and scintillation detectors, highlighting the influence of the retarding grid on background noise at low implantation energies for the HPGe detector.

6. Discussion and Outlook

The primary achievement of this thesis is the successful development and implementation of a new experimental apparatus for studying positron reemission phenomena at the Setup for Low-Energy Positron Experiments (SLOPE) facility. This included the design of a galvanically isolated active sampleholder with a custom DC-DC charge pump, regulated by a robust PID control loop, and the integration of a Retarding Field Analyzer (RFA) with an electrostatic lens system designed with COMSOL Multiphysics. The subsequent measurements on tungsten, nickel, and platinum samples have not only demonstrated the functionality of this new setup but also highlighted the complexities of the task.

The reemission spectrum measured for the W(111) sample, while showing a clear signal, did not exhibit the sharp, well-defined peak expected from the emission of thermalized positrons. Instead, a broad energy spectrum was observed, with a maximum reemission energy determined to be $-1.87(10)$ eV. This value is significantly lower than the literature value for the positron work function of clean W(111), which is approximately $\phi^+ = -2.6$ eV [23]. The broadening of the spectrum cannot be explained by thermal effects alone and therefore suggests that the sample surface was affected by oxidation or the presence of adsorbates, which are known to alter the surface dipole layer and trap positrons. Furthermore, the energy shift could be attributed to a contact potential difference between the sample material and the retarding grid. Due to the complex geometry of the lens system and the different metals and alloys involved, an analytical determination of this contact potential wasn't possible. Therefore, the energy axis of the Retarding Field Analyzer (RFA) will need to be calibrated using a reference sample with a known work function, that ideally has been cleaned via in-situ annealing.

This interpretation is further supported by the measurements on the nickel and platinum samples. For nickel, only a small increase in the scintillation detector count rate was observed at low retarding potentials, a signal significantly weaker than that from tungsten. The expected positron work function for nickel is approximately $\phi^+ = -1.5$ eV [24]. It is plausible that the combination of this lower work function and a contact potential higher than 1.5 V shifts the entire thermalized positron spectrum to energies below 0 V. The small observed signal could originate from epithermal positrons. These are positrons that are reemitted before fully thermalizing in the bulk. Similarly, the platinum measurement, though compromised by experimental interruptions, showed no distinct spectrum from thermalized positrons. With an electron work function different from tungsten [25, 23], the contact potential for platinum could be larger, also

6. Discussion and Outlook

shifting its expected spectrum ($\phi^+ \approx -2.2$ eV [24]) out of the currently measurable range.

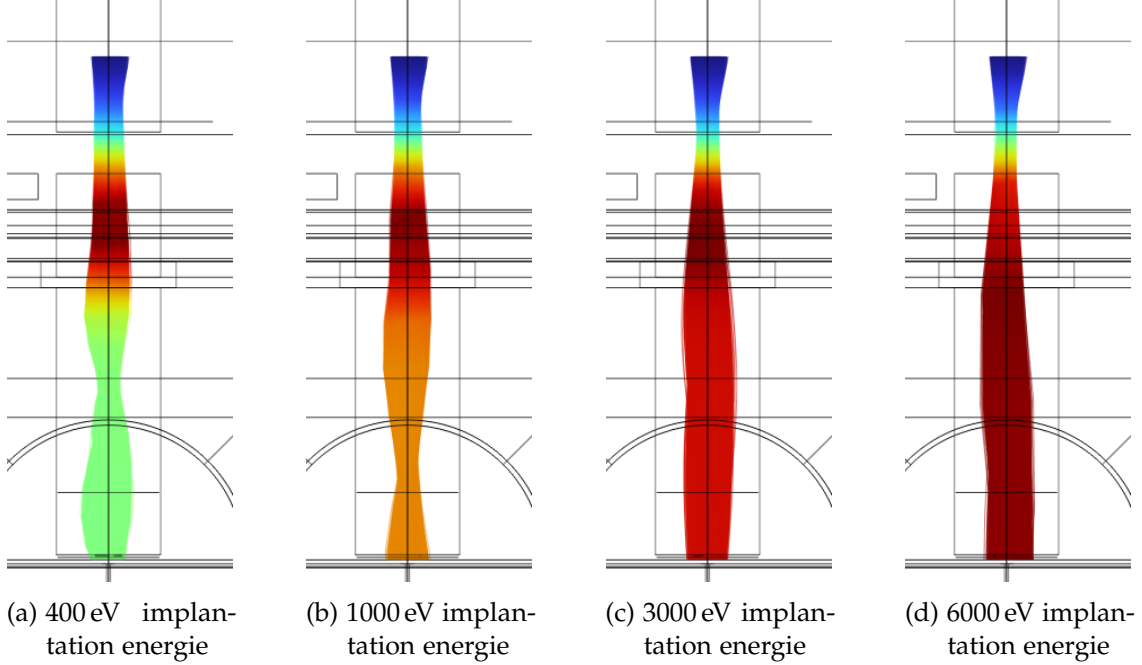


Figure 6.1.: Simulations of the incoming positron beam profile for various implantation energies. The simulations illustrate that the beam shape changes significantly at lower energies, which likely contributes to the instrumental artifacts observed in the yield measurements below 1000 eV.

The reemission yield measurements for all samples consistently showed an increase in remoderated positrons at lower implantation energies. While this general trend is consistent with the theoretical expectation that positrons implanted closer to the surface have a higher probability of diffusing back, the detailed behavior was more complex. The data revealed a particularly steep increase in yield below approximately 1.5 keV, a feature that cannot be explained by the thermal reemission model alone. This steep rise is now understood to be a significant contribution from epithermal positrons, which scatter back to the surface before fully thermalizing. As demonstrated with the tungsten data, a combined model incorporating both thermal diffusion and epithermal scattering provides a much better qualitative agreement with the measurements across all samples.

However, this physical model does not account for all observed features. A notable anomaly was still present in the count rates for implantation energies below 1000 eV, where a local dip in the reemitted signal was observed before the steep epithermal rise. This feature is not related to the reemission process itself but is likely a systematic artifact of the beam transport optics. As illustrated by the COMSOL simulations in Figure 6.1,

the profile of the incoming positron beam changes significantly at low energies. The strong attractive potential of the dump lens can more significantly deflect the low-energy primary beam, altering its focus onto the sample and causing the observed fluctuations in annihilation rates. Therefore, the measured yield at low energies is a superposition of a real, enhanced epithermal emission signal and an instrumental artifact caused by beam defocusing.

This interpretation is further supported by the background measurements performed on the copper sample plate. The weak signal observed there, which was most prominent at low energies, can be interpreted as epithermal, positron reemission from the copper surface itself. Future work should therefore focus on a systematic characterization of the beam optics at different energies to deconvolve the instrumental artifacts from the true reemission yield, allowing for a more quantitative analysis of the epithermal contribution.

Based on the presented findings, several areas for future investigation and system refinement can be outlined. A primary recommendation is the integration of an in-situ sample preparation method, such as high-temperature annealing. This would enable the creation of atomically clean surfaces, allowing for more accurate and reproducible measurements. Characterization of a clean reference sample would also provide a basis for calibrating the RFA's energy scale by determining existing contact potentials, thereby allowing precise measurements of positron work functions.

Further characterization of the beam optics will be required, specifically regarding the influence of the dump lens voltage on the primary beam profile at low implantation energies. A systematic study of this parameter could lead to optimized voltage settings, ensuring a stable and consistent beam profile across the operational energy range. Additionally, improvements to the RFA design itself may be considered. Incorporating supplementary grids, analogous to designs utilized in Low-Energy Electron Diffraction (LEED) systems, could potentially generate a more uniform and well-defined retarding field, reducing susceptibility to external stray fields.

In summary, this thesis has successfully established a measurement setup for retarding field analysis at the SLOPE facility. This includes the implementation of the active sampleholder, which provides PID-controlled voltage biasing for the retarding grid. While initial measurements have highlighted limitations primarily related to beam optics, the presented work identifies steps for future improvements.

Acknowledgments

First, I would like to thank Prof. Dr. Christoph Hugenschmidt for providing me with the idea and opportunity for this thesis and for his initial guidance and support. A special thanks goes to B.Sc. Max Suhr. He not only introduced me to the slope experiment but also dedicated many days with me at the MLL to install the new setup. His help with the COMSOL simulations and his constant availability for questions and guidance are not taken for granted. I am especially thankful for the opportunity to use his labbeam control software, which spared me countless long trips to the MLL. I would also like to thank Dr. Francesco Guatieri for his expertise and insightful answers, as well as his initial design of the active sampleholder. The nice and encouraging talks in the office were always a source of motivation. My thanks also go to Sebastian Vohburger for manufacturing all the parts for the lens system with great quality and always on time. Finally, I wish to thank the rest of the NEPOMUC group for creating a pleasant and supportive atmosphere. The welcoming environment made my time here truly enjoyable.

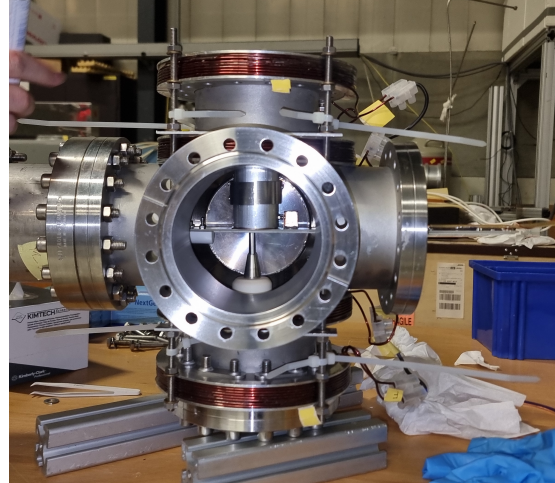
Appendices

A. Experimental Setup

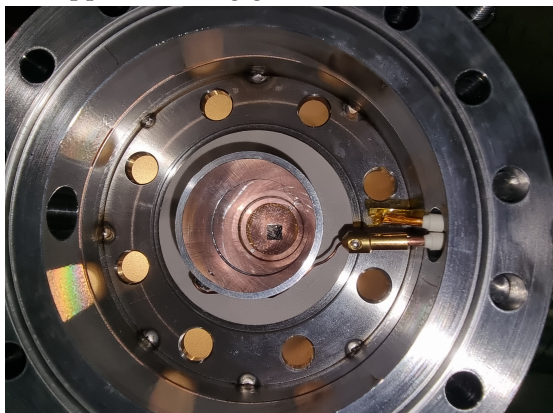
A. Experimental Setup



(a) The active sampleholder assembly with the copper retarding grid installed.



(b) Side view of the sample chamber during assembly, showing the sampleholder positioned between the electrostatic lens system and the iron pin.



(c) Top-down view into the assembled sample chamber. The electrostatic lens system, retarding grid, and the HV feedthrough (right) are visible.



(d) The fully assembled Labbeam.

Figure A.1.: Photos of the experimental setup, showing (a) the active sampleholder, (b) its installation into the sample chamber, (c) a top-down view of the chamber internals, and (d) the complete Labbeam.

B. Reemission Yield Estimation

An attempt was made to perform a preliminary estimation of the absolute reemission yield for the measured samples. The reemission yield, Y , is defined as the ratio of the number of reemitted low-energy positrons, $I_{\text{reemitted}}$, to the number of primary positrons incident on the sample surface, I_{sample} :

$$Y = \frac{I_{\text{reemitted}}}{I_{\text{sample}}} \quad (\text{B.1})$$

To estimate this value, both the numerator and the denominator must be determined from experimental parameters and simulations.

The number of positrons incident on the sample, I_{sample} , is a fraction of the total incoming beam intensity, I_{beam} . The total intensity delivered to the sample position is approximately 8.8×10^4 positrons per second [18]. However, due to the energy-dependent nature of the beam optics, not all of these positrons strike the sample. COMSOL simulations of the beam profile at various energies suggest that the fraction of the beam hitting the sample, f_{sample} , lies between 65% and 93%. This provides a lower and upper bound for the incident positron rate:

$$I_{\text{sample}} = I_{\text{beam}} \cdot f_{\text{sample}} \quad (\text{B.2})$$

The number of reemitted positrons, $I_{\text{reemitted}}$, cannot be measured directly but is inferred from the coincidence count rate, C_{meas} , recorded by the BGO scintillation detectors aimed at the beam dump. The relationship between the measured rate and the reemitted intensity depends on the total probability of detecting a coincidence event for each annihilation, $\varepsilon_{\text{total}}$:

$$C_{\text{meas}} = I_{\text{reemitted}} \cdot \varepsilon_{\text{total}} \quad (\text{B.3})$$

The total detection probability, $\varepsilon_{\text{total}}$, is a product of the probability that the annihilation photons strike the detectors and their intrinsic efficiency for detecting those photons. The probability of one of the two isotropically emitted 511 keV photons striking a detector is determined by the fractional solid angle, Ω_{frac} . This is the ratio of the detector's front-face area to the surface area of a sphere whose radius is the distance d from the annihilation point:

$$\Omega_{\text{frac}} = \frac{\pi r_{\text{det}}^2}{4\pi d^2} = \frac{r_{\text{det}}^2}{4d^2} \quad (\text{B.4})$$

The intrinsic efficiency, ε_{int} , for a single 511 keV photon is the probability that it interacts within the detector volume. This is modeled using the Beer-Lambert law,

B. Reemission Yield Estimation

where μ is the linear attenuation coefficient for 511 keV photons in the detector material and t is the detector thickness:

$$\varepsilon_{\text{int}} = 1 - e^{-\mu t} \quad (\text{B.5})$$

The specific parameters for the BGO scintillators and HPGe detectors used in these calculations are listed in Table B.1.

Table B.1.: Detector parameters used for the reemission yield estimation.

Parameter	BGO Scintillator	HPGe Detector	Unit
Radius (r_{det})	2.5	2.9	cm
Thickness (t)	5.0	6.8	cm
Distance (d)	8.0	4.5	cm
Linear Attenuation Coeff. (μ)	0.906	0.063	cm ⁻¹

Furthermore, the retarding grid itself is not perfectly transparent to positrons. This grid has a geometric transmission efficiency, T_{grid} , estimated to be 90%. This efficiency impacts the calculation twice: it reduces the number of primary positrons reaching the sample and subsequently reduces the number of reemitted positrons that pass back through to the dump lens. The total coincidence detection probability for a single annihilation event was therefore modeled as:

$$\varepsilon_{\text{total}} = 2 \cdot \varepsilon_{\text{int}}^2 \cdot \Omega_{\text{frac}} \quad (\text{B.6})$$

By combining these expressions and accounting for the double pass through the grid, the absolute reemission yield Y can be calculated from the measured coincidence rate:

$$Y = \frac{C_{\text{meas}}}{I_{\text{beam}} \cdot f_{\text{sample}} \cdot T_{\text{grid}}^2 \cdot 2 \cdot \varepsilon_{\text{int}}^2 \cdot \Omega_{\text{frac}}} \quad (\text{B.7})$$

This calculation was performed for all samples across the measured energy range, using both the lower (65%) and upper (93%) estimates for f_{sample} to establish bounds for the yield. However, the resulting values for the reemission yield were consistently very low, remaining below 1% for all materials and implantation energies within both the lower and upper bounds.

While it cannot be definitively ruled out that the reemission efficiency of the ex-situ prepared samples is this low, it is more likely that the simplified model does not account for all loss mechanisms. For instance, the transmission efficiency of the retarding grid, estimated here at 90% based on its geometry, could be effectively lower due to local electric field distortions near the grid wires that deflect low-energy positrons. Other potential sources of discrepancy include positron losses during transport from the sample to the beam dump. Therefore, while this framework establishes a method for estimation, a more meaningful and accurate determination of the absolute reemission yield would require more detailed characterization of the experimental setup and better simulations to account for these loss factors.

Acronyms

NEPOMUC NEutron induced POsitron source MUniCh

ACAR Angular Correlation of Annihilation Radiation

DBS Doppler Broadening Spectroscopy

PALS Positron Annihilation Lifetime Spectroscopy

PAS Positron Annihilation Spectroscopy

ADC Analog-to-Digital Converter

MCU Microcontroller Unit

PIC Peripheral Interface Controller

PID Proportional-Integral-Derivative

PWM Pulse-Width Modulation

HPGe High-Purity Germanium

HV High-Voltage

IR Infrared

RFA Retarding Field Analyzer

UHV Ultra-High Vacuum

SLOPE Setup for Low-Energy Positron Experiments

List of Figures

1.1.	Makhovian profiles for positrons in Tungsten, Nickel and Platinum at various implantation energies. The parameters used for the Makhovian profiles are taken from [8].	5
1.2.	Schematic of the potential energy for an electron (top) and a positron (bottom) at a metal-vacuum interface [10]. The diagram illustrates the bulk chemical potentials (μ_- and μ_+), the surface dipole barrier (Δ), and the resulting work functions (ϕ_- and ϕ_+). The negative work function for the positron ($\phi_+ < 0$) leads to its spontaneous emission from the surface.	8
1.3.	β^+ spectrum of ^{22}Na before and after moderation. Figure taken from Hugenschmidt 2016 [10]	9
1.4.	Forward and backward reemission yield as a function of incident positron energy for a 1000 Å thick W(100) film. The forward yield (labeled with squares) peaks at an optimal energy, while the backward yield (labeled with circles) decreases monotonically. Figure adapted from Chen et al. [12]	11
1.5.	Focusing the beam (diagonal lines) conserves brightness by trading beam area for angular divergence. Remoderation (horizontal lines) is a non-conservative process that creates a smaller effective source size while restoring low angular divergence, thus increasing brightness.. Figure from Schultz and Lynn [3].	13
2.1.	Schematic drawing of the Labbeam with designations of coils and valves. Figure taken from Springl 2023 [17]	15
2.2.	Rendered view of the sample chamber.	17
2.3.	Detailed view of the simulated electric potential in the retarding grid region. A clear retarding field gradient can be seen, allowing only positrons with sufficient kinetic energy to overcome the potential barrier to pass through.	19
2.4.	COMSOL Multiphysics simulations of the sample chamber. (a) The electric potential with the sample at -3000 V, the retarding lens (L1) at +3 V (relative to the sampleholder), and the dump lens (L2) at -3600 V. (b) The magnitude of the magnetic flux density generated by external coils, which confines the beam. (c) Trajectories of the incoming positron beam focused onto the sample. (d) Trajectories of reemitted positrons that overcome the retarding potential, showing their precession and annihilation on the dump lens.	20

3.1. Schematic of the custom DC-DC charge pump. A PWM signal ("Drive") from the MCU switches the transistor (Q1), allowing energy to be stored in the inductors (L1, L2) during its on-state. When Q1 switches off, the stored energy is transferred through the diode (D8) to a low-pass filter stage (C26, C28, R19, R21), which generates a smooth DC output voltage. This output is then scaled down by a voltage divider (R13, R21) and monitored at the "ADC2" pin, providing the necessary feedback for the control system.	22
3.2. Step response of the DC-DC charge pump for various voltage transitions. The system settles to within 1% of the target value in under 2s for all transitions.	24
3.3. Voltage drift of the chargepump over two hours.	25
3.4. Dependence of the charge pump output voltage on the illumination LED supply current. The measurement was performed with a constant PWM duty cycle to isolate the effect of input power.	26
3.5. Mapping of the charge pump output voltage as a function of PWM high-time and low-time. The non-linear relationship necessitates a closed-loop control system. The red-highlighted regions indicate the two operating regimes used by the PID control system as described in the next section, optimized for high-voltage and low-voltage control, respectively.	28
3.6. Output voltage of the charge pump as a function of PWM high-time for the two distinct operating regimes used by the PID controller. The regime with a 75 μ s low-time (orange) offers a wide control range and a less steep voltage decline, making it suitable for the high-voltage range (0.6 V to 7.8 V). In contrast, the regime with a 375 μ s low-time (blue) enables fine control down to 0 V but exhibits a steeper voltage change at higher high-times, making it ideal for the low-voltage range (< 0.6 V). The observed voltage cutoff at 7.81 V is due to the maximum measurable voltage of the onboard ADC.	29
4.1. Two-dimensional maps of coincidence count rates as a function of the C4H and C4V correction coil currents at 3 keV. The top row (a, b) shows data from the HPGe detectors, indicating annihilations on the sample. The bottom row (c, d) shows data from the scintillation detectors, indicating annihilations on the dump lens. Measurements were performed with retarding grid potentials of 0 V (left column) and 7 V (right column) to distinguish between incident and reemitted positrons.	32
4.2. Difference maps of the scintillation detector coincidence count rates (0V data minus 7V data). Both plots isolate the signal from reemitted positrons, showing a maximum that indicates the optimal coil settings for the setup. On the left is the low-resolution scan, and on the right is the high-resolution scan.	33

4.3. Coincidence count rates of the Scintillator (Blue) and the Germanium (Green) Detector Pair as a function of the voltage ΔV_{Lens} between sample and dump lens for 3 keV (left) and 5.5 keV (right) implantation energy. A clear peak in the scintillator signal is observed at $\Delta V_{\text{lens}} \approx -100$ V in both scans, confirming the optimal setting is independent of the sample voltage. Each data point represents a 3-minute long measurement.	34
5.1. Integral energy spectrum of W(111) measured across the full voltage range of the active sample holder. The coincidence count rate at the scintillators (SLA x SLB) and the HPGe (OAH x OAB) is shown as a function of the retarding grid potential. Above approximately 3 V, the signal reaches a constant background level, marking the relevant energy window for further measurements.	39
5.2. Integral and differential energy spectra of remoderated positrons from W(111). (a) Three independent measurements showing no systematic error. The primary y-axis (left) shows the signal from the scintillation detectors (SLA x SLB), while the secondary y-axis (right) shows the signal from the HPGe detectors (OAH x OAB). (b) The combined and smoothed integral spectrum (green line) with the raw summed data points (blue markers). The corresponding differential energy spectrum (dN/dE) is shown as a dashed blue line.	40
5.3. Determination of the cutoff energy for W(111) using Poisson statistics. The plot shows the probability of the background process producing the observed count at each retarding grid potential. The sharp drop indicates the start of the true positron signal. The cutoff energy is determined to be 1.87 ± 0.1 V, marked by the red dashed line and confidence interval.	40
5.4. Positron reemission yield for W(111) as a function of implantation energy. (a) and (b) show the raw coincidence count rates for the HPGe and scintillation detectors, respectively, at 0 V and 7 V retarding grid potentials. (c) and (d) display the difference in count rates for the HPGe and scintillation detectors, isolating the signal from reemitted positrons.	42
5.5. Comparison of the measured reemission yield for W(111) with theoretical models. The solid blue line represents the calculated backscattering yield considering only thermalized positrons, which fails to match the data at low energies. The dashed red line includes an additional contribution from epithermal positrons, modeled according to Britton 1988 [11]. The combined model shows significantly better agreement with the measured data (orange points), particularly below 2 keV.	43
5.6. Integral energy spectrum of remoderated positrons from Nickel (Ni) at 1000 eV implantation energy. The coincidence count rate at the scintillators (SLA x SLB) and the HPGe (OAH x OAB) is shown as a function of the retarding grid potential. A slight increase in scintillator count rate is visible at lower voltages.	44

5.7. Reemission yield for Nickel (Ni) as a function of implantation energy. (a) and (b) show the raw coincidence count rates for the HPGe and scintillation detectors, respectively, at 0 V and 7 V retarding grid potentials. (c) and (d) display the difference in count rates for the HPGe and scintillation detectors, isolating the signal from reemitted positrons.	45
5.8. Integral energy spectrum of remoderated positrons from Platinum (Pt) at 3000 eV implantation energy. The blue and green points represent data collected before and after a server interruption, respectively. A systematic shift is visible, making the data unsuitable for detailed analysis.	46
5.9. Reemission yield for Platinum (Pt) as a function of implantation energy. (a) and (b) show the raw coincidence count rates for the HPGe and scintillation detectors, respectively, at 0 V and 7 V retarding grid potentials. (c) and (d) display the difference in count rates for the HPGe and scintillation detectors, isolating the signal from reemitted positrons.	48
5.10. Background spectrum measured with no sample installed. The coincidence count rate at the scintillators (SLA x SLB) and the HPGe (OAH x OAB) is shown as a function of the retarding grid potential. The count rates are constant, indicating no influence of the retarding grid on background noise.	49
5.11. Background yield measured with no sample installed. (a) and (b) show the raw coincidence count rates for the HPGe and scintillation detectors, respectively, at 0 V and 7 V retarding grid potentials. (c) and (d) display the difference in count rates for the HPGe and scintillation detectors, highlighting the influence of the retarding grid on background noise at low implantation energies for the HPGe detector.	50
6.1. Simulations of the incoming positron beam profile for various implantation energies. The simulations illustrate that the beam shape changes significantly at lower energies, which likely contributes to the instrumental artifacts observed in the yield measurements below 1000 eV.	52
A.1. Photos of the experimental setup, showing (a) the active sampleholder, (b) its installation into the sample chamber, (c) a top-down view of the chamber internals, and (d) the complete Labbeam.	60

Bibliography

- [1] P. A. M. Dirac. "A Theory of Electrons and Protons." In: *Proceedings of the Royal Society of London. Series A, Containing Papers of a Mathematical and Physical Character* 126 (Aug. 1930), pp. 360–365. ISSN: 0950-1207. DOI: 10.1098/rspa.1930.0013.
- [2] C. D. Anderson. "The Positive Electron." In: *Physical Review* 43 (Mar. 1933), pp. 491–494. DOI: 10.1103/PhysRev.43.491.
- [3] P. J. Schultz and K. G. Lynn. "Interaction of positron beams with surfaces, thin films, and interfaces." In: *Rev. Mod. Phys.* 60 (3 July 1988), pp. 701–779. DOI: 10.1103/RevModPhys.60.701.
- [4] B. Straßer. "Aufbau einer Anlage zur positroneninduzierten Auger-Elektronenspektroskopie." Dissertation. München: Technische Universität München, 2002.
- [5] C. Hugenschmidt, C. Piöchacz, M. Reiner, and C. Schrekkenbach. "The NEPOMUC upgrade and advanced positron beam experiments." In: *New Journal of Physics* 14.5 (2012), p. 055027. ISSN: 1367-2630. DOI: 10.1088/1367-2630/14/5/055027.
- [6] M. R. Dodenhöft. "Instrumentation of the positron diffractometer at NEPOMUC and measurements on epitaxial graphene grown on 6H-SiC(0001)." PhD thesis. Technical University of Munich, 2022.
- [7] P. G. COLEMAN. "INTRODUCTION: A BRIEF HISTORY OF POSITRON BEAMS." In: *Positron Beams and Their Applications*, pp. 1–10. DOI: 10.1142/9789812817754_0001. eprint: https://www.worldscientific.com/doi/pdf/10.1142/9789812817754_0001.
- [8] J. Dryzek and P. Horodek. "GEANT4 simulation of slow positron beam implantation profiles." In: *Nuclear Instruments and Methods in Physics Research Section B: Beam Interactions with Materials and Atoms* 266.18 (2008), pp. 4000–4009. ISSN: 0168-583X. DOI: <https://doi.org/10.1016/j.nimb.2008.06.033>.
- [9] M. J. Puska and R. M. Nieminen. "Theory of positrons in solids and on solid surfaces." In: *Rev. Mod. Phys.* 66 (3 July 1994), pp. 841–897. DOI: 10.1103/RevModPhys.66.841.
- [10] C. Hugenschmidt. "Positrons in surface physics." In: *Surface Science Reports* 71.4 (2016), pp. 547–594. ISSN: 0167-5729. DOI: <https://doi.org/10.1016/j.surfrep.2016.09.002>.

Bibliography

- [11] D. T. Britton, P. C. Rice-Evans, and J. H. Evans. "Epithermal effects in positron depth profiling measurements." In: *Philosophical Magazine Letters* 57.3 (1988), pp. 165–169. doi: 10.1080/09500838808203766. eprint: <https://doi.org/10.1080/09500838808203766>.
- [12] D. M. Chen, K. G. Lynn, R. Pareja, and B. Nielsen. "Measurement of positron reemission from thin single-crystal W(100) films." In: *Phys. Rev. B* 31 (7 Apr. 1985), pp. 4123–4130. doi: 10.1103/PhysRevB.31.4123.
- [13] S. Ghosh, J. R. Danielson, and C. M. Surko. "Energy distribution and adiabatic guiding of a solid-neon-moderated positron beam." In: *Journal of Physics B: Atomic, Molecular and Optical Physics* 53.8 (Mar. 2020), p. 085701. doi: 10.1088/1361-6455/ab7642.
- [14] D. A. Fischer, K. G. Lynn, and D. W. Gidley. "High-resolution angle-resolved positron reemission spectra from metal surfaces." In: *Phys. Rev. B* 33 (7 Apr. 1986), pp. 4479–4492. doi: 10.1103/PhysRevB.33.4479.
- [15] L. Mathes. "Depth Resolved Doppler-Broadening Spectroscopy on Oxides Using a Table-Top Positron Beam." Master's Thesis. Garching, Germany: Technical University of Munich, 2020.
- [16] M. Suhr. *Positronium Formation on Polymer Surfaces Studied by Low-Energy Positrons*. Bachelor's Thesis in Physics. Garching, Germany, Sept. 2023.
- [17] C. Springl. *Determination of the Atomic-Vacancy Concentration in Quenched Tungsten by Doppler-Broadening Spectroscopy of the Positron Annihilation Line*. Bachelor's Thesis in Physics. Original German title: *Bestimmung der atomaren Leerstellenkonzentration in abgeschrecktem Wolfram mithilfe der Doppler-Verbreiterungsspektroskopie der Positronenannihilationslinie*. Sept. 2023.
- [18] L. Mathes, M. Suhr, V. V. Burwitz, D. R. Russell, S. Vohburger, and C. Hugenschmidt. "Surface and near-surface positron annihilation spectroscopy at very low positron energy." In: *Journal of Instrumentation* 19.11 (Nov. 2024), P11026. doi: 10.1088/1748-0221/19/11/P11026.
- [19] C. Inc. COMSOL. 2020.
- [20] K. Brenner. *In-operando positron beam experiments under extreme conditions*. Bachelor's Thesis in Physics. Garching, Germany, Oct. 2020.
- [21] W. R. Leo. *Techniques for Nuclear and Particle Physics Experiments: A How-To Approach*. Springer Science & Business Media, 2012. ISBN: 978-3-642-57919-6. doi: 10.1007/978-3-642-57920-2.
- [22] K. Porth. *Hydrogen Loading of Nickel-based Superalloys Investigated by Positron Annihilation Spectroscopy*. Bachelor's Thesis in Physics. Untersuchung von Wasserstoffbeladenen Nickelbasislegierungen mit Positronen Annihilations Spektroskopie. July 2025.

- [23] R. J. Wilson and A. P. Mills. "Positron and positronium emission from tungsten (111)." In: *Phys. Rev. B* 27 (7 Apr. 1983), pp. 3949–3954. doi: 10.1103/PhysRevB.27.3949.
- [24] C. Hugenschmidt, B. Straßer, and K. Schreckenbach. "Investigation of positron work function and moderation efficiency of Ni, Ta, Pt and W(1 0 0)." In: *Applied Surface Science - APPL SURF SCI* 194 (June 2002), pp. 283–286. doi: 10.1016/S0169-4332(02)00135-6.
- [25] L. A. DuBridge. "The Photoelectric and Thermionic Work Functions of Outgassed Platinum." In: *Phys. Rev.* 31 (2 Feb. 1928), pp. 236–243. doi: 10.1103/PhysRev.31.236.